JOURNAL OF GEOPHYSICAL RESEARCH, VOL. 106, NO. D22, PAGES 28,751–28,770, NOVEMBER 27, 2001

Regional air pollution and its radiative forcing: Studies with a single-column chemical and radiation transport model

R. J. Park,[1] G. L. Stenchikov,[2] K. E. Pickering,[1] R. R. Dickerson,[1]
D. J. Allen,[1] and S. Kondragunta[3]

Abstract. This study focuses on the effects of subgrid (on general circulation model (GCM) scales) convective venting of the planetary boundary layer to the free troposphere and on the interactive effects of aerosols, ozone, UV actinic flux, and radiative forcing of climate. We developed a single-column chemical transport model (SCCTM) consistent with the global Goddard Earth Observing System (GEOS) GCM and Chemical Transport Model (CTM). The SCCTM includes vertical transport by convection, turbulent mixing, a flexible photochemical scheme, and interactive calculations of radiative fluxes and photolysis rates. The model is designed as a chemical and physical core to be used in a completely interactive GCM. At this time it is driven by data from the GEOS Data Assimilation System archived by the Data Assimilation Office at NASA Goddard. We simulated an ozone/aerosol pollution episode in the Baltimore-Washington region and a convective event in the central United States. These physically distinct case studies provide a thorough test for the chemical scheme and physical parameterizations employed in the SCCTM. The ozone episode simulation showed strong sensitivity to aerosol optical depth, with increased average PBL ozone due to the effects of aerosols on photolysis rates. Observed aerosols produced a surface cooling of up to 100 W m^{-2} and stabilized the atmosphere suppressing convection. In the convective event over Oklahoma a squall line carried pollutants into the free troposphere increasing O_3 by up to 35 ppbv and peroxyacetylnitrate by up to 400 pptv. The maximum instantaneous radiative forcing due to this ozone reached 0.75 W m^{-2} at the tropopause level. Accurate representation of the interaction among particles, trace gases, radiation, and convection is essential for global climate models.

1. Introduction

In this paper we study aerosol-ozone-climate interactions focusing on the effects of convection and aerosols on tropospheric ozone and on its radiative forcing. Because of the patchy distribution of sources and short life cycle of aerosols and ozone precursors, aerosol and ozone effects have a pronounced regional-scale component. Therefore we begin our development of an appropriate modeling system by studying regional-scale pollution with a Single-Column Chemical Transport Model (SCCTM). We compare our calculations to observations and cloud-resolving model calculations to test parameterizations and evaluate the role of various physical mechanisms.

Transport and chemical transformation of optically active trace gases and aerosols modify the large-scale distributions of chemical species and affect their global budgets, thereby having important implications for the chemical composition of the atmosphere and its radiative properties. Being a main atmospheric oxidizing component and an optically active constituent, ozone plays an important role in the climate system along with CO_2, N_2O, CH_4, and CFCs. Ozone in the stratosphere and troposphere shields the Earth's ecosystems from UV radiation. However, increased mixing ratios of ozone near the surface are harmful to human health and damage crops and other plants. As a strong absorber of UV and longwave radiation, ozone affects Earth's radiative budget and climate [*Wang et al*., 1980, 1993; *Lacis et al*., 1990; *Haigh*, 1996]. The formation of tropospheric ozone is highly nonlinear [e.g., *Liu et al*., 1987] and depends on numerous factors.

Vertical mixing of ozone precursors in the troposphere is an important process because the rate of ozone production is affected nonlinearly by the precursor concentrations, as well as by actinic fluxes that depend on altitude and ozone mixing ratios. Deep convection is one of the most effective transport mechanisms that vertically redistribute short-lived trace gases. Convection rapidly vents constituents emitted in the planetary boundary layer (PBL) to the free troposphere, where their lifetime increases because loss mechanisms such as dry deposition, scavenging by precipitation, and reaction with the hydroxyl radical (OH) are largest in the PBL.

Lelieveld and Crutzen [1994] suggested that convective overturning causes a net decrease in total tropospheric ozone concentration. They conducted global calculations and found that in the clean marine environment, convective downdrafts transport upper tropospheric air (enriched in O_3 because of downward transport from the stratosphere and in NO_x because of stratospheric input and lightning) toward the Earth's surface, where loss mechanisms of those constituents are strongest.

[1]Department of Meteorology, University of Maryland, College Park, Maryland, USA.
[2]Department of Environmental Sciences, Rutgers University, New Brunswick, New Jersey, USA.
[3]Office of Research and Applications, NOAA/NESDIS, Camp Springs, Maryland, USA.

Paper number 2001JD001182.
0148-0227/01/2001JD001182$09.00

However, calculations for rural and urban areas over land [*Chatfield and Delany*, 1990; *Pickering et al*., 1990, 1992a, 1992b] have shown that deep convection can cause the enhancement of ozone production in the free troposphere because the photochemical O_3 yield per NO_x molecule increases as a result of dilution [*Liu et al*., 1987]. Therefore the convective lifting of NO_x from the boundary layer into the free troposphere enhances the formation of O_3 in the upper and middle troposphere. A prolonged lifetime of precursors and the enhanced production of O_3 in the free troposphere imply an increase in total tropospheric column O_3 as a result of convection over polluted areas. The changes of column content and vertical distribution of ozone in the troposphere affect absorption of radiation in the atmosphere and therefore could cause radiative forcing of climate.

Aerosol particles in the atmosphere scatter and absorb solar radiation. Their optical properties depend on their size and composition. Submicron sulfate aerosols are effective at scattering of solar radiation and have a cooling effect because of reflection of solar radiation back to space [*Charlson et al*., 1992; *Kiehl and Briegleb*, 1993]. Carbonaceous aerosol and mineral dust can effectively absorb solar radiation and heat the PBL [*Penner et al*., 1998; *Ramanathan*, 1999]. In the infrared spectrum, aerosols mostly absorb radiation and act like a greenhouse gas although typically the optical depth at long wavelengths is significantly less than that in the solar wavelength band. The impact of these aerosols on the Earth's radiative balance and climate (aerosol radiative forcing) has been studied extensively [*Houghton et al*., 1996]. However, aerosol-climate effects remain uncertain because of large temporal and spatial variability of aerosol radiative properties and the complexity of physical processes responsible for aerosol formation and loss. Aerosols affect tropospheric chemistry, providing surfaces for heterogeneous reactions [*Jacob*, 2000]. Along with the radiative effect on climate, aerosols also modify the UV actinic flux and the rate of photochemical reactions [*Jacobson*, 1997; *Dickerson et al*., 1997; *Jacobson*, 1998; *Liao et al*., 1999] that drive the chemistry of the atmosphere. *Dickerson et al*. [1997] showed that UV-scattering particles, in spite of reflection of radiation, can strongly increase the density of the photons in the PBL and accelerate photochemical reactions and ozone production. On the contrary, UV-absorbing aerosols remove the photons from the PBL and decrease ozone production and near-surface ozone mixing ratios [*Dickerson et al*., 1997; *Kondragunta*, 1997; *Jacobson*, 1998]. Aerosols also modify surface temperature and atmospheric stability because of their radiative effects [*Jacobson*, 1998; *Gamazaychikov et al*., 1998; *Kiehl et al*., 1999].

Our ultimate goal is to incorporate improved tropospheric ozone chemistry and aerosol effects into the Goddard Earth Observing System general circulation model (GEOS GCM) and conduct interactive chemical transport and radiation calculations. For this purpose we are working to combine the Stretched-Grid GEOS GCM [*Fox-Rabinovitz et al*., 1997; 2001] and Stretched-Grid GEOS CTM [*Allen et al*., 2000]. The stretched-grid design allows us to address specifically the interaction of small-, regional-, and global-scale processes. As part of the development of the global three-dimensional (3-D) coupled chemical transport model and general circulation model we have designed a Single-Column Chemical Transport Model that represents the physical and chemical core of the 3-D chemical transport model. Here we use the SCCTM for case study calculations, which help us to evaluate the role of various competing effects, to test different chemical schemes, and to evaluate vertical mixing and radiative transport parameterizations for GCM use. We study interactions of tropospheric ozone chemistry and radiative forcing of climate, focusing on the effects of aerosols and convective mixing. It is important to test the SCCTM in a variety of conditions. Therefore we use observations from two physically different episodes: The first case is a stagnant air mass having high ozone and aerosol concentrations in the PBL, and the second case is characterized by instability and deep convection that enhances upper tropospheric ozone mixing ratios. We have also studied the radiative forcing of observed aerosols and of the increase in upper tropospheric O_3 mixing ratios caused by deep convection.

In section 2 we describe the SCCTM. In section 3 we present the application of the SCCTM for two regional air pollution studies. Conclusions of the study are formulated in section 4.

2. Model Description

One-dimensional chemical models with eddy diffusional mixing have been widely used for studying chemical processes in the atmosphere [e.g., *Thompson and Cicerone*, 1986]. The Single-Column Model (SCM) approach for testing parameterizations in GCMs and for interpretation of field campaign measurements was proposed by *Randall et al*. [1996]. This approach is based on using a complete physical description of the processes in an atmospheric column adopted from a parent GCM in combination with observed advective fluxes of heat and moisture. The SCM approach is closely tied to the Radiative-Convective Model (RCM) approach [*Manabe and Wetherald*, 1967; *Ramanathan*, 1981]. *Stenchikov and Robock* [1995] used a RCM/SCM for process analysis of the diurnal asymmetry of global warming and provided a review of previous studies. Here we developed a single-column chemical and radiative transport model using parameterizations from the GEOS GCM [*Takacs et al*., 1994] and the 3-D Goddard Chemical Transport Model (GCTM) [*Lin and Rood*, 1996; *Allen et al*., 1996]. The model calculates vertical transport, turbulent mixing, and chemical transformations of constituents in the atmospheric column, as well as radiative transport accounting for aerosols and optically active gaseous species. A similar approach was employed by *Wang et al*. [2000] based on the Goddard Institute for Space Studies (GISS) GCM parameterizations to study biomass burning effects over the tropical Pacific.

The SCCTM is driven by the assimilated data from the GEOS Data Assimilation System (DAS) [*Schubert et al*., 1993]. Here we use output from the GEOS-1 system with a resolution of 2° in latitude by 2.5° in longitude and 20 vertical layers in a sigma coordinate system extending from the surface to 10 hPa. The SCCTM could be easily reconfigured to use output from the current GEOS-3 system with $1° \times 1°$ horizontal resolution and 48 vertical layers. To improve the description of the PBL in the SCCTM we added five additional layers (0.977, 0.965, 0.938, 0.922, and 0.874 sigma values, equivalent to ~990, 978, 951, 935, and 887 hPa when surface pressure is 1013 hPa) in the lowest part of the model, typically allowing a total of eight layers to be simulated below 900 hPa. The GEOS-1 data are interpolated to these additional layers. The SCCTM calculation is performed for a $2° \times 2.5°$ grid cell centered on a latitude and longitude selected by the user. The GEOS DAS data are horizontally interpolated to this location. The meteorological input parameters used to conduct model calculations include

surface pressure, temperature, specific humidity, and turbulent kinetic energy at 0000, 0600, 1200, and 1800 UT, 3-hour-averaged PBL depth, 6-hour-averaged cloud mass flux, and convective cloud detrainment. The SCCTM could be forced by the large-scale advection of chemical constituents calculated using the GEOS DAS fields if detailed distributions of chemical species were available. Below we give detailed descriptions of the physical processes implemented in the SCCTM.

2.1. Chemistry

SMVGEAR II is a sparse matrix vectorized Gear-type first-order differential equation solver [*Jacobson*, 1995]. It includes flexible kinetic and photolytic chemical reaction packages. The software allows easy addition and removal of reactions and species. The current chemical scheme includes 96 chemical species (all of which are transported) accounting for O_3, NO_x, and hydrocarbon chemistry. To focus the chemical scheme on tropospheric ozone photochemistry we disregard all predominantly stratospheric reactions and reactions involved with chlorine, sulfur, and bromine from the full set of kinetic and photolytic reactions that came from *Jacobson* [1994]. We include heterogeneous loss of N_2O_5 on aqueous aerosols assuming pseudo-first-order reaction in this calculation. The final scheme includes 200 kinetic and 19 photolytic reactions.

2.2. Convection and Turbulent Mixing

Vertical transport of trace gases and aerosols by deep convection is parameterized in the SCCTM using the cumulus mass flux and detrainment calculated with the Relaxed Arakawa-Schubert (RAS) algorithm [*Moorthi and Suarez*, 1992; *Arakawa and Schubert*, 1974] and archived by the GEOS DAS. The RAS algorithm is used to parameterize convection in all versions of the GEOS GCM. Therefore the convective forcing and the dynamical fields used for driving the SCCTM are consistent.

The change of mixing ratio of a particular chemical constituent as a result of convective mixing is determined by solving iteratively a coupled linear system that defines the upward mass flux due to convection across the edges of model layers [*Allen et al*., 1996]. The moist convective mixing is allowed to start through the fixed cloud base at the 0.954 sigma layer. Complete mixing below the cloud base is assumed. The upward cloud mass flux is balanced by subsidence outside of the model cloud but within the GCM grid box.

The contribution of turbulence to vertical mixing of constituents is calculated using a vertical conservative diffusion equation

$$\frac{\partial \pi q}{\partial t} = \frac{\partial}{\partial \sigma} D(\sigma) \frac{\partial \pi q}{\partial \sigma}, \tag{1}$$

where q is the constituent mixing ratio, $\pi = p_{\mathrm{sfc}} - p_{\mathrm{top}}$, p_{sfc} is the surface pressure, p_{top} is the pressure at the model top, and $D(\sigma)$ is the vertical diffusion coefficient which is a function of the vertical coordinate $\sigma = (p - p_{\mathrm{top}})/\pi$. We use the Crank-Nicholson scheme to solve the diffusion equation which is a tridiagonal matrix system given as

$$a_j q_{j-1}^{n+1} + b_j q_j^{n+1} + c_j q_{j+1}^{n+1} = q_j^n, \qquad j = 1, \ldots, N, \tag{2}$$

where j is the number of the model layers (from 1 to 25 in this simulation), and n is the time step index. The calculation of turbulent mixing with the Crank-Nicholson scheme has second-order accuracy in space and time, is numerically efficient, and absolutely stable. The vertical diffusion coefficient is calculated using turbulent kinetic energy from the GEOS-1 DAS assimilated data. The direct usage of assimilated data for turbulent mixing has the advantage of consistency with the dynamic fields [*Helfand et al*., 1991].

2.3. Emission and Dry Deposition

We assume that emissions and dry deposition take place only in the bottommost layer of the model. The increase in concentration c_g due to emission is calculated with the equation

$$\frac{\partial c_g}{\partial t} = \frac{J_e}{z_1}, \tag{3}$$

where J_e (molecules $\mathrm{cm}^{-2}\,\mathrm{s}^{-1}$) is the emission flux and z_1 is the height of the bottommost layer.

The changes of concentrations due to the dry deposition are calculated using the deposition flux J_d, which is parameterized as the product of the concentration c_g and the deposition velocity v_d:

$$\frac{\partial c_g}{\partial t} = -\frac{v_d c_g}{z_1} = -\frac{J_d}{z_1}. \tag{4}$$

The deposition velocities for different species are adopted from *Sander and Crutzen* [1996] and are constant throughout the model runs.

2.4. Wet Scavenging

We use a modified form of the scheme of *Allen et al*. [2000] for removing soluble species from the atmosphere in precipitation. We have applied this scheme to HNO_3, H_2O_2, and H_2CO in the SCCTM. Loss of the soluble species is assumed to occur continually as a first-order loss process dependent on altitude. In addition, these species are removed more rapidly on an episodic basis during periods of convective precipitation. For example, for nitric acid a lifetime of 5 days is assumed from the surface to 600 hPa with the lifetime increasing to ~50 days at 200 hPa. In convective precipitation the lifetime is assumed to be 1 day at sigma levels where liquid droplets are plentiful (temperature greater than 258 K). Lifetimes for rainout for the other species are taken from *Warneck* [1988].

2.5. Radiative Transfer Calculations

Solar radiation not only provides the energy for the climate system but also drives photochemical reactions. In this section we discuss our techniques for calculating radiative forcing by aerosols and trace gases and for calculating photolysis rates in a polluted atmosphere using observed aerosol characteristics.

2.5.1. Photolysis rate calculations. We improved the radiation model of *Dickerson et al*. [1997] for calculating photolytic reaction constants to include the 19 photolytic reactions shown in Table 1. The radiation model uses the Discrete Ordinate Radiative Transfer (DISORT) scheme [*Stamnes et al*., 1988] for calculating solar radiances for 16 angular ordinates. The MIE package [*Wiscombe*, 1980] is implemented for calculating aerosol optical properties: extinction coefficient, asymmetry factor, phase function, and single scattering albedo. Typically, we calculate the photolysis rates off-line, but in some cases we conduct the radiative calculations interactively. Interactive calculations are time-consuming but allow us to account for time variations of ozone and aerosol. For the more economic off-line calculations the solar irradiances and mean ac-

Table 1. Photochemical Reactions and the Sources of the Spectral Data Used in the Photolysis Rate Coefficients Calculations[a]

Reaction	Absorption Cross Section	Quantum Yield
$O_3 + h\nu \rightarrow O(^3P) + O_2$	M	D
$O_3 + h\nu \rightarrow O(^1D) + O_2$	M	D
$H_2O_2 + h\nu \rightarrow OH + OH$	D	D
$NO_2 + h\nu \rightarrow NO + O(^3P)$	D	D
$NO_3 + h\nu \rightarrow NO_2 + O(^3P)$	W	W
$NO_3 + h\nu \rightarrow NO + O_2$	W	W
$N_2O_5 + h\nu \rightarrow NO_2 + NO_3$	D	D
$HONO + h\nu \rightarrow OH + NO$	D	A
$HNO_3 + h\nu \rightarrow OH + NO_2$	D	D
$HO_2NO_2 + h\nu \rightarrow HO_2 + NO_2$	A	A
$HO_2NO_2 + h\nu \rightarrow OH + NO_3$	A	A
$HCHO + h\nu \rightarrow H + HCO$	D	D
$HCHO + h\nu \rightarrow CO + H_2$	D	D
$CH_3OOH + h\nu \rightarrow CH_3O + OH$	A	A
$CH_3CHO + h\nu \rightarrow CH_3 + HCO$	A	A
$CH_3ONO_2 + h\nu \rightarrow CH_3O + NO_2$	A	A
$CH_3O_2NO_2 + h\nu \rightarrow CH_3O_2 + NO_2$	A	A
$CH_3COCH_3 + h\nu \rightarrow CH_3CO + CH_3$	A	A
$CH_3COCHO + h\nu \rightarrow CH_3CO + HCO$	A	A

[a]A, *Atkinson et al.* [1997]; D, *DeMore et al.* [1997]; M, *Molina and Molina* [1986]; W, *Wayne et al.* [1991].

tinic flux at each layer are precalculated at 10 different solar zenith angles. The spectral aerosol characteristics are approximated with 1-nm resolution from 176 to 700 nm. The use of a spectral resolution of 1 nm allows us to calculate actinic flux with sufficient accuracy at the wavelengths where the absorption cross section changes rapidly and where most photochemical reactions of interest occur.

We use the solar constant (400–700 nm) obtained from the National Solar Observatory [*Kurucz et al.*, 1984] and from the Solar Ultraviolet Spectral Irradiance Monitor (SUSIM) observation [*VanHoosier et al.*, 1988] for shorter wavelengths. Ozone profiles and the total column ozone amount (325 DU) were obtained from a blend of Stratospheric Aerosol and Gas Experiment (SAGE) data and ozonesonde observations [*Wellemeyer et al.*, 1997] in the midlatitudes and were used for both episode simulations. Stratospheric ozone is kept fixed in all experiments. Changes in tropospheric ozone due to chemical production have little effect on photolysis rates because stratospheric ozone absorbs almost all of the UV radiation. Rayleigh scattering cross section σ_s is calculated using the approximation from *Liou* [1992]. The albedo of most natural and manmade materials is low in the ultraviolet region and increases with wavelength. We assumed land surface albedo of 8% in the ultraviolet, which is an averaged value determined from the experimental spectral reflectance data of *Coulson and Reynolds* [1971]. The computation of photolysis rates requires absorption cross-section and primary quantum yield data for each species and the spectral region of interest. The absorption cross-section and quantum yields [*DeMore et al.*, 1997] are averaged over 1-nm wavelength intervals. The references to absorption cross-section and quantum yield data used in calculating photolysis rates constants are presented in Table 1. The effect of clouds on photolysis rate frequencies is parameterized according to *Chang et al.* [1987] and *Brasseur et al.* [1998]. Correction factors due to cloud in the parameterization are functions of cloud optical depth, cloud fraction, and solar zenith angle. GEOS-1 DAS data, however, do not provide cloud optical depth explicitly. Therefore we specified cloud optical depth based on cloud type and temperature [*Takacs et al.*, 1994]. Cloud fraction F at any level is also calculated using time-averaged random and maximum overlapped cloudiness with a line-of-site calculation given by

$$F = 1 - (1 - \mathrm{MAX}_p^{p'}\,[\mathrm{CLMO}_p]) \prod_p^{p'} (1 - \mathrm{CLRO}_p),$$

where CLMO is maximum overlapped cloudiness, CLRO is random overlapped cloudiness, p is the pressure at current level, and p' is the model top pressure, or the model surface pressure [*Takacs et al.*, 1994].

2.5.2. Radiative forcing calculation. We implemented on-line radiation transport calculations in the SCCTM using the radiative transfer parameterizations from the GEOS GCM [*Chou*, 1992; *Chou and Suarez*, 1994; *Chou et al.*, 1995]. The parameterizations for solar and thermal infrared radiative transfer account for N_2O, CH_4, CFC11, CFC12, CFC22, H_2O, CO_2, O_3, and aerosols. In the solar radiation routine the effects of the absorption and scattering due to clouds and aerosols, as well as Rayleigh scattering, are included. We assumed land surface albedo of 16% in the visible and in the near infrared. We use the radiative transfer parameterization to compute radiative forcing due to changes in the vertical distribution of optically active trace gases and aerosols. The radiative forcing calculations presented here are performed at each time step using the computed trace gas mixing ratios. The atmospheric variables from the GEOS-1 DAS and the vertical distribution of gases including water vapor are provided at every time step.

3. Regional Air Pollution Plume Case Studies

In this section we present the results of two physically different case studies to better understand how aerosols and convection can influence photochemical ozone production in the troposphere and affect climate and to test SCCTM performance. Case 1 was conducted for a highly polluted urban region for a summer period with high O_3 mixing ratios in the PBL. In case 2 we look at the formation of a pollution plume in the upper troposphere resulting from a deep convective episode in the central United States.

3.1. Case 1: Chemical Formation of a PBL Pollution Plume in the U.S. East Coast Urban Region

During the July 12–15, 1995, period high O_3 mixing ratios were registered in the Baltimore-Washington area and throughout the eastern United States [*Dickerson et al.*, 1997; *Ryan et al.*, 1998]. Ozone observations at the Greenbelt, Maryland, monitoring site show a peak hourly average O_3 mixing ratio of 110 ppbv on July 12, increasing to 160 ppbv on July 15. A number of monitors observed exceedances of the National Ambient Air Quality Standard (NAAQS) for O_3 (120 ppbv averaged over 1 hour) throughout the eastern part of United States during this period. Meteorological conditions on July 12–15 were hot and stable, typical for high smog episodes in this area. A strong upper air ridge built over the Midwest, which along with a surface high-pressure system in the eastern United States, brought favored conditions for high O_3 occurrence [*Ryan et al.*, 1998]. Synoptic-scale subsidence accompanying the high-pressure system inhibited cloud formation and intensified atmospheric stability so that vertical mixing of low-level emissions was suppressed, and therefore photochemical

activity was enhanced. This pollution episode was also characterized by high concentrations of aerosols. By late on July 15 a weak trough moved over the top of the ridge, bringing a weak surface front southward and terminating the high-ozone episode.

We have applied the SCCTM for simulating this high-ozone episode. The circulation for July 12–15 was characterized by weak horizontal transport. Therefore we neglect the large-scale horizontal advection of pollutants for the period of simulation although the effect of circulation on meteorological fields (such as adiabatic heating due to subsidence) is included in the GEOS-DAS fields used to drive the SCCTM calculations. No convection was observed at the Greenbelt site. Therefore we did not invoke the convective parameterization in the SCCTM in this case. We also assumed clear skies for all radiative calculations in this case, because very little cloudiness was observed. *Dickerson et al*. [1997] previously applied the variable-grid urban airshed model (UAM-V) to study this high-ozone episode. The UAM-V employs a different chemical scheme and solver than does the SCCTM, including an extended version of the Carbon Bond Mechanism Version IV (CB-IV) [*Gery et al*., 1989].

To calculate the ozone precursor distributions we used the Ozone Transport Assessment Group (OTAG) emission inventories [*SAI*, 1995], which were developed specifically for July 12–15, 1995. The inventory includes data for 13 chemical species averaged for 1-hour periods with horizontal resolution of 0.5° in longitude by 0.33° in latitude. The species for which we used the OTAG emissions are as follows: NO, NO_2, CO, CH_3OH, C_2H_5OH, HCHO, CH_3CHO, C_2H_4, PAR (single-bonded one-carbon-atom surrogate), OLE (carbon-carbon double bonds surrogate), xylene, toluene, and isoprene.

3.1.1. Effects of observed aerosols on photochemistry. We calculate actinic flux and photolysis rates as a function of altitude with and without urban aerosols; we use these photolysis rates in the SCCTM simulations to evaluate the effect on photochemical O_3 production. We use finer vertical resolution than that used by *Dickerson et al*. [1997] (12 layers below 4 km versus 7 layers in the UAM-V and 5 layers below 0.5 km versus 4 layers in the UAM-V), which enables us to better resolve the vertical transport and chemistry in the PBL, where the complex chemistry and dynamical mixing take place, and to better describe the ozone production above the PBL.

In this study we take advantage of routine Sun photometer observations conducted on the grounds of the NASA Goddard Space Flight Center (GSFC) in Greenbelt, Maryland [*Holben et al*., 1998], and we use aerosol size-number distribution retrieved from the radiances measured on July 15. In our calculations we use the same refractive index, $m = 1.45 - 0.005i$, as in the size distribution retrieval algorithm. This refractive index agrees well with the estimates for the East Coast aerosol composed predominantly of sulfates, organic compounds, and nitrates [*Hegg et al*., 1997]. Using the size-number distribution and refractive index we conduct Mie calculations to obtain aerosol optical properties such as the extinction coefficient, asymmetry factor, phase function, and single scattering albedo ω. For the July 15 case the aerosol optical depth τ was ~2.0 at 380 nm, which we consider to be representative of aerosol optical depths in the Baltimore-Washington region for the conditions on this date [*Dickerson et al*., 1997].

The vertical distribution of aerosols has a significant effect on radiative transport and hence on photolysis rates. The current observations only provide the column-averaged aerosol size-number distribution; therefore we assume that aerosols with the observed optical depth are confined and mixed uniformly in the lowest 1-km layer. Therefore the aerosol optical depth decreases linearly with height up to the top of the 1-km aerosol layer. No aerosols are assumed to exist above this altitude. The NO_2 and O_3 photolysis rates as a function of height are shown in Figure 1 for a solar zenith angle of 10°. The aerosols (with single scattering albedo $\omega = 0.96$ and asymmetry factor $g = 0.70$ for 380 nm according to Mie calculations using the given refractive index) decrease $j(NO_2)$ at the surface. However, $j(NO_2)$ increases with height because of the increase in actinic flux due to aerosol backscattering. Comparisons of direct measurement of $j(NO_2)$ at the Greenbelt site and the calculated values using Mie theory and the DISORT model were performed over a broad range of aerosol optical depths and solar zenith angles and showed excellent agreement with observations [*Kelley et al*., 1995]. The impact of aerosols on $j(O_3 \rightarrow O[^1D])$ is similar to that on $j(NO_2)$. The clear sky $j(O_3 \rightarrow O[^1D])$ increases with altitude showing a maximum at ~500 hPa and then decreases with altitude (not shown here). The decrease in the $j(O_3 \rightarrow O[^1D])$ results because the decrease in O_3 absorption due to decreasing temperature with altitude outweighs the increase in actinic fluxes with increasing altitude. Our calculated clear sky $j(O_3 \rightarrow O[^1D])$ is in very good agreement with $j(O_3 \rightarrow O[^1D])$ from *Dickerson et al*. [1982] and *Liao et al*. [1999].

In this calculation we consider hydrolysis of N_2O_5 on aerosols. The first-order rate constant [see *Jacobson*, 1994] for heterogeneous loss is a strong function of reaction probability and aerosol surface area. The reaction probability has a large uncertainty (in the range 0.01–1). We used a most probable value of 0.1 recommended by *Jacob* [2000]. The total aerosol surface area is calculated using the observed size-number distribution and is uniformly distributed in the 1-km aerosol layer. To quantify the radiative effect of aerosols on photochemical ozone production in the PBL we conducted calculations including heterogeneous removal of N_2O_5 for both aerosol and no-aerosol conditions, as well as calculated the effect of heterogeneous chemistry itself.

Ozone production is highly sensitive to concentrations of ozone precursors [e.g., *Liu et al*., 1987]. Therefore model initial conditions may be a crucial factor for ozone evolution in the simulation. We performed sensitivity calculations over two different periods of time (starting on July 9 and July 11) using initial background concentrations found in rural eastern U.S. environments. We found that the SCCTM solution quickly reached the same regime regardless of the starting time of calculations. It shows that in our case there is only moderate sensitivity to initial conditions.

For the July 12–15 case study the ozone precursor emissions were calculated by averaging OTAG emissions at grid points within 1° (1.25°) in the north-south (east-west) direction of the Greenbelt, Maryland, site (39.01° in latitude, −76.87° in longitude) for each corresponding day. Over 24 data grids of OTAG emissions are generally included in the averaged emission used in the SCCTM calculation. The use of averaged emissions may result in underestimating the peak ozone mixing ratio because the spatial variation of precursor emissions is smoothed over our grid cell.

Figure 2 shows the differences in ozone mixing ratios calculated with and without aerosols for the July 12–15 Greenbelt case. The results are averaged below 1000 m and below 500 m. The dotted line represents the effect at the surface (the lowest

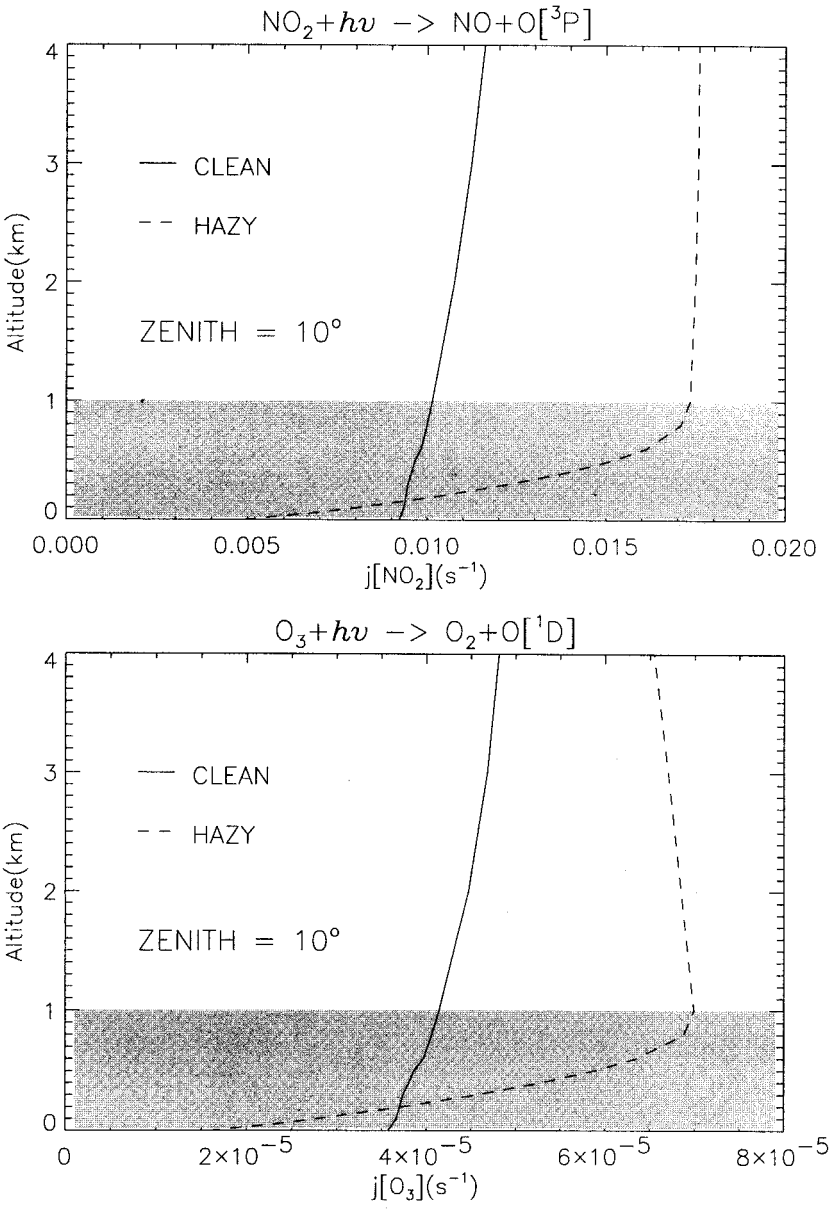

Figure 1. Calculated $j(NO_2)$ and $j(O_3)$ as a function of height for solar zenith angle 10°. The dashed line denotes the profile of $j(NO_2)$ and $j(O_3)$ for clear-sky conditions with aerosol in the boundary layer (below 1 km), and the solid line denotes the profile for conditions without aerosol.

model layer). Model results show that UV-scattering particles generally increase ozone production within the 1000-m layer but decrease surface ozone by ~15 ppbv on July 15. The magnitude of the increase in our calculated ozone averaged below 500 m (~4 ppbv) at noon is in reasonable agreement with the variable-grid urban airshed model (UAM-V) calculations (~5 ppbv) of *Dickerson et al.* [1997]. The results show a strong dependence of ozone production on aerosol effects at different altitudes within the PBL, though the scattering aerosols result in an increase in bulk O_3 production in the PBL.

There is a distinct diurnal cycle of ozone changes due to aerosols as shown in Figure 2. The peak of the ozone increase is near noon, and the maximum ozone decrease is before sunset or just after sunrise. The ozone decrease is due to the fact that the decrease in near-surface $j(NO_2)$ due to boundary layer aerosols is larger at high solar zenith angle. The maximum decrease in $j(NO_2)$ at the lowest model layer (indicated as "surface" in Figure 2) is −75% relative to no-aerosol conditions for solar zenith angle 80°. Under the hazy sky condition, the ratio of diffuse to direct radiation in the total actinic fluxes increases relative to that for the no-aerosol condition. For small solar zenith angles the increase in diffuse flux compensates for the attenuation of solar direct flux by aerosols. For a high solar zenith angle the diffuse radiation available for photolysis near the surface decreases because attenuation of radiation dominates owing to an increase in effective optical depth [*Dickerson et al.*, 1997].

Calculations with and without including N_2O_5 hydrolysis on aerosols show that N_2O_5 removal decreased NO_x mixing ratios during the night and early morning and hence decreased calculated O_3 by up to 3 ppbv averaged over the PBL on July 15, compared with no heterogeneous loss of N_2O_5. This effect

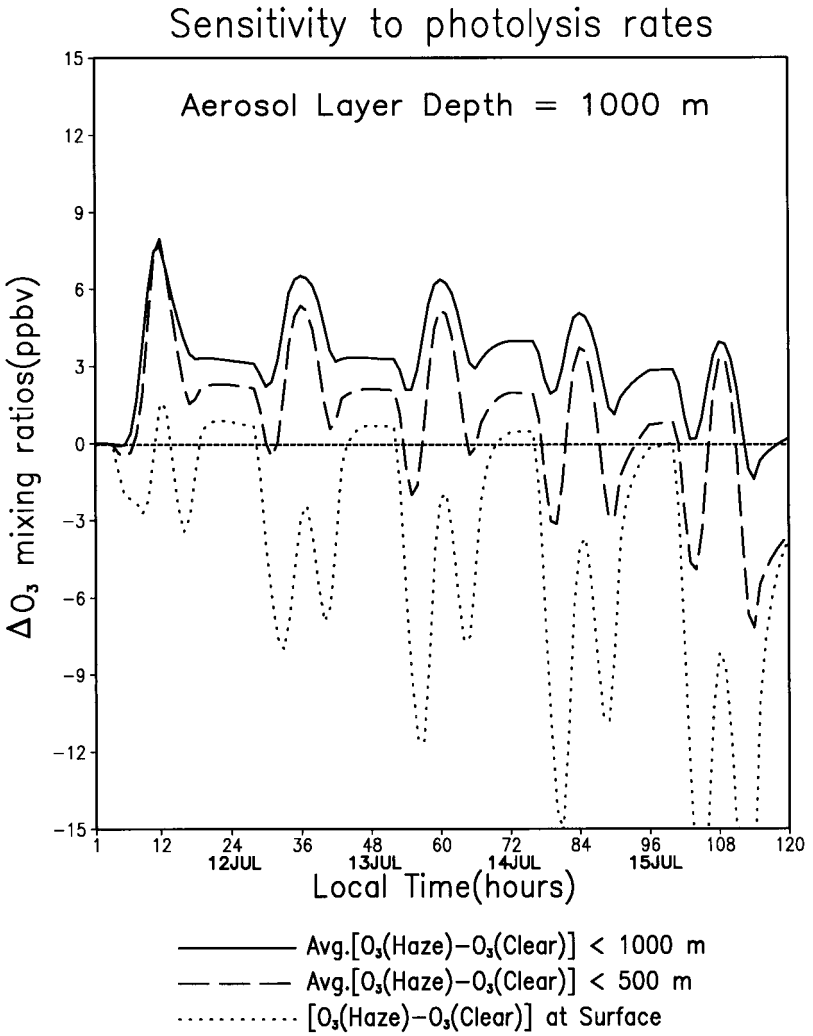

Figure 2. Difference in O_3 as a function of time between clear- and hazy-sky condition with aerosol loading of 1-km depth. Lines represent the changes in ozone averaged below 1 km (solid line), 0.5 km (long dashed line), and dotted line is at the lowest model layer. Refer to Figure 3 for approximate magnitudes of surface ozone mixing ratios.

turned out to be comparable in magnitude and opposite in sign with the radiative enhancement of ozone production due to the aerosol-induced increase in photolysis rates. It shows that both effects are equally important and should be accounted for in detail. However, at the present time there is considerable uncertainty with the representation of heterogeneous chemistry in the models [*Jacob*, 2000].

3.1.2. Effect of diurnal variation of aerosol vertical distribution on ozone production in the PBL. The fixed-in-time vertical distribution of aerosols used in section 3.1.1 is a simplification. Because of diurnal variation of the PBL depth and turbulent mixing (as well as aerosol sources), the aerosol vertical distribution changes during the day. The aerosol diurnal variation affects the ozone production differently throughout the day. To evaluate the role of this effect, we implemented a diurnal cycle of aerosol distribution in the SCCTM and conducted photolysis rate calculations interactively accounting for the vertical ozone and aerosol profiles provided by the SCCTM. For this simulation we set the depth of the aerosol layer equal to that of the PBL, which varies with time, and we assumed a linear decrease of aerosol optical depth with height (equivalent to a vertically uniform aerosol concentration distribution) up to the top of the PBL where it vanishes.

Figure 3 shows the results of the interactive model calculations with and without aerosols in comparison with surface ozone observations. The model results presented show the ozone concentrations at the lowest model layer. The larger ozone mixing ratios on July 15 from the model interactive calculation with diurnal variations of aerosol vertical distribution are in better agreement with the observations than the interactive model results with no aerosols. The increase in photolysis rates on July 15, especially $j(NO_2)$, relative to the previous calculations with the fixed aerosol layer results from the shrinkage of the PBL depth and hence the aerosol layer (see Figure 4), caused by strong subsidence. The evolution of the PBL height from GEOS-1 DAS (Figure 4) shows good agreement with successive radiosonde observations [*Ryan et al.*, 1998] during this episode. With a shallower PBL the actinic flux increases owing to the increase in aerosol scattering near the surface. Under these conditions a deeper column of atmosphere has enhanced photolysis. A very slight increase in surface ozone is noted for the simulation with aerosol on July 14,

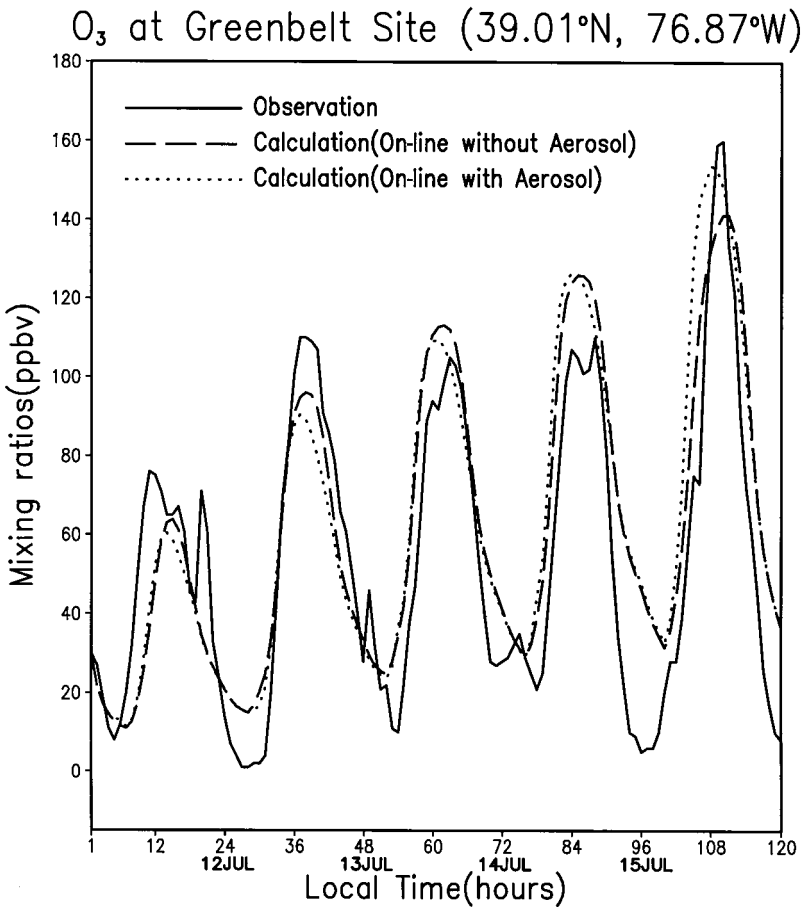

Figure 3. Time series of surface O_3 at Greenbelt site. Solid line is O_3 observed, dotted line is O_3 calculated with diurnally varying aerosols in the boundary layer, and dashed line is O_3 calculated without aerosols.

which had a 300 m deeper PBL than did July 15. July 11, 12, and 13 had considerably deeper boundary layers, and the simulations with aerosol produced decreased ozone at the surface. This result is partly attributable to our assumption of vertically uniform aerosol distribution in the PBL, which works better for a shallow boundary layer. In a deep boundary layer on July 11–13 we likely underestimate aerosol mixing ratios near the surface, which causes lower ozone amounts in our calculations. In addition, aerosol data from July 15 were used throughout the simulation. We suspect that some of the disagreement on

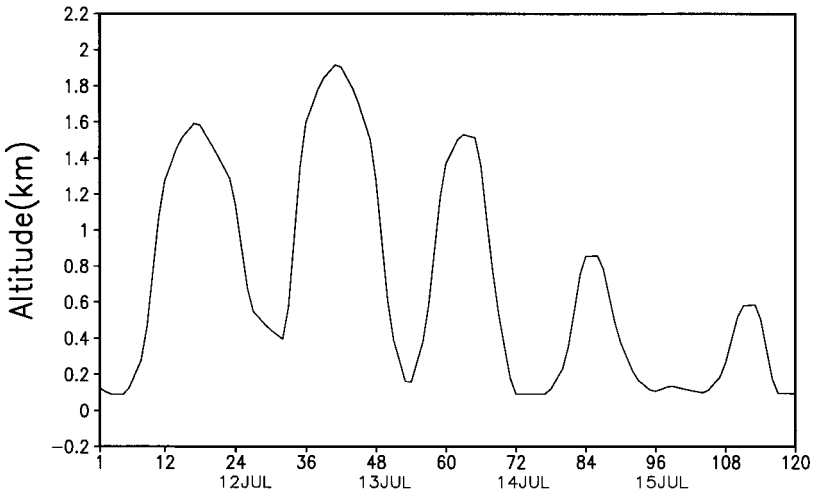

Figure 4. Planetary boundary layer depth from GEOS-1 Data Assimilation System used as input for the single-column chemical transport model.

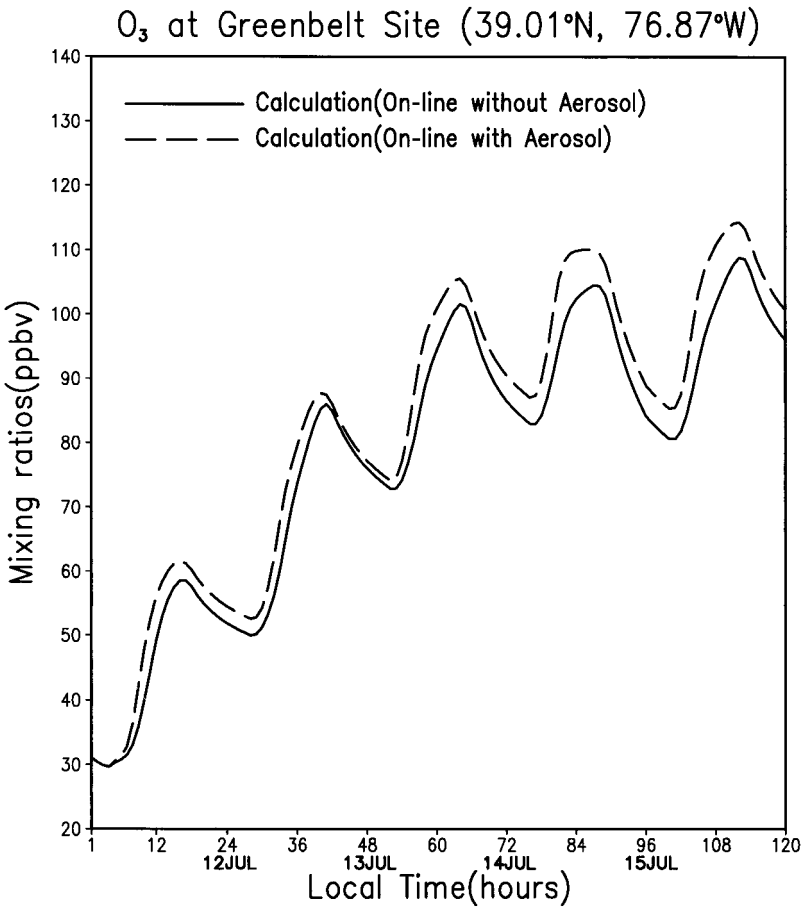

Figure 5. Ozone mixing ratios vertically averaged from the surface to ~2 km altitude in the simulation with diurnally varying aerosol and in the simulation without aerosols.

other days may also arise from differing aerosol amount and characteristics on those days.

The interactive model calculations with variable aerosol layer captures the important observed effect of the dramatic increase of O_3 mixing ratios on July 15 compared to the previous days. For example, our previous calculations with a fixed 1-km aerosol layer showed that aerosols caused a decrease in near-surface ozone mixing ratios.

Comparison between calculations and observations for species other than O_3 is not possible, because other species were not measured at the Greenbelt site. However, the nearest station with NO measurements (Fort Meade, 16 km to the north) shows good agreement with the model on all days for the timing of the NO peak. It also shows good agreement of the NO mixing ratios on two days (~8 ppbv on July 11 and ~1 ppbv on July 15), but the model underestimated the observed values on the other three days. NO mixing ratios would be expected to be much more spatially variable than O_3 in the real atmosphere because NO is directly emitted by automobiles. Therefore NO will be highly dependent on the sampling location relative to major highways and on traffic volumes on the specific days. Given the daytime underestimates of NO, we suspect that NO emissions at night may be too low in the model. There appears to be insufficient NO to titrate ozone to the observed low values.

Figure 5 shows the time series of ozone mixing ratios averaged over the layer from the surface to ~2 km for the aerosol and no-aerosol simulations. At all times the vertically averaged ozone mixing ratio is larger in the simulation in which aerosols are considered than in the simulation without aerosols. The difference varies from ~3 to 8 ppbv. This result clearly demonstrates the importance of the inclusion of aerosols in photochemical simulations of polluted boundary layers.

3.1.3. Climate radiative forcing of observed aerosols. We use the radiative routines implemented in the SCCTM to calculate the radiative forcing of aerosols and ozone. The difference of radiative fluxes at the tropopause, computed with and without the aerosols using the same meteorological fields from GEOS DAS, is the aerosol radiative forcing of the atmosphere at any given time as per the definition of instantaneous radiative forcing [see *Houghton et al.*, 1996]. Here we use the term "aerosol radiative forcing" in a wider sense and assume that it includes the changes of instantaneous radiative fluxes caused by aerosols at all model levels. We conduct calculations for clear-sky conditions because very little cloudiness was observed.

In the context of this study, aerosols affect climate by absorbing and scattering radiation; they also affect the photochemical production of O_3 (through modification of photolysis rates). Altered O_3 mixing ratios, in turn, produce their own effects on the radiative balance. We do not consider here the aerosol indirect radiative forcing through the effect on cloud microphysics. Because the vertical distribution of aerosol does not have an important effect on radiative forcing at the surface

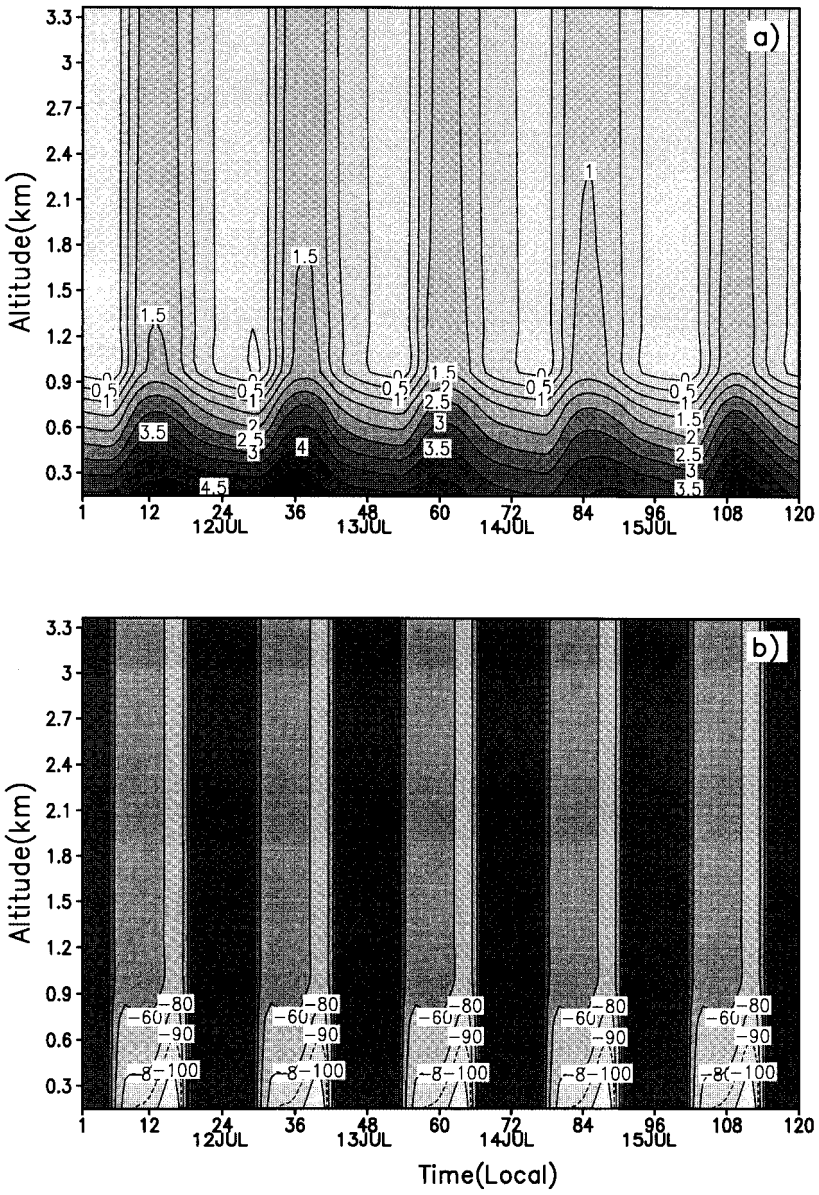

Figure 6. Radiative forcing due to the presence of aerosols for July 11–15, 1995, at Greenbelt, Maryland. (a) Changes in net longwave fluxes (downward) and (b) changes in net shortwave fluxes (downward) with aerosols versus with no aerosols (W m^{-2}).

and we do not have detailed information about aerosol vertical distribution from observations, we assume that aerosols are uniformly distributed in the lowest 1-km model layer as in the initial photolysis rate calculation. Our results show that the effect of boundary layer aerosols outweighed that of the resulting change of ozone on the radiative balance. In these simulations we calculate aerosol radiative parameters (optical depth, single scattering albedo, and asymmetry factor) using the three size distributions observed on July 15, 1995, and the refractive index from the retrieval procedure (see section 3.1.1). The Mie calculations for all three size distributions yielded single scattering albedo $\omega = 0.96$, and asymmetry parameter $g = 0.69 \pm 0.03$ for 380 nm. The radiative forcing calculation is insensitive to small variations in size distribution. The third parameter needed for radiative forcing calculations is aerosol optical depth, which we take as $\tau = 2.0$ for 380 nm in the UV in accordance with the observations taken during the day. In the visible at 550 nm the corresponding observed optical depth is $\tau = 1.28$ (AERONET, http://aeronet.gsfc.nasa.gov/), single scattering albedo $\omega = 0.96$, and asymmetry parameter $g = 0.65 \pm 0.03$.

We also provide the calculated O_3 to the radiative transfer calculation at each time step, although the effect of changes in these ozone amounts is negligible. The same meteorological fields from the GEOS DAS that were used in the chemical transport calculations are also used in the radiative computations. Figure 6 shows changes in the net downward longwave (LW) and shortwave (SW) fluxes (i.e., the radiative forcing caused by aerosols). Aerosols absorb longwave radiation emitted from the Earth's surface and increase the downward irradiance within the aerosol layer. The peak increase in net longwave flux up to 4.5 W m^{-2} very close to the surface. However,

Table 2. Optical Properties Calculated With Aerosol Size-Number Distributions Measured on July 15, 1995, and the Resulting Shortwave Radiative Forcing at the Surface[a]

Radiative Parameters	Time of Measurement 1614 UT 1114 LT	1714 UT 1214 LT	1814 UT 0114 LT
Solar zenith angle, deg	21.004°	17.558°	22.48°
Optical depth (τ at 380 nm)	1.26	1.74	1.57
Single scattering albedo (ω)	0.96	0.96	0.96
Asymmetry parameter (g)	0.70	0.66	0.72
Shortwave forcing at surface,[b] W m^{-2}	−59.6	−80.4	−75.2
Shortwave forcing at surface,[c] W m^{-2}	−41.3	−58.2	−51.9

[a]UT, universal time; LT, local time.
[b]Used single scattering albedo of 0.96 as calculated.
[c]Used single scattering albedo of 1.00 for purely scattering aerosols.

the changes in net downward shortwave fluxes are much larger, and reach −100 W m^{-2} near the surface in the afternoon. Diurnal average of radiative cooling on July 15 is −50.7 W m^{-2} at the surface. This extremely strong radiative surface cooling is partly compensated by adiabatic heating due to subsidence induced by the anticyclone. The surface temperature continues to climb during the episode, although it may have been even hotter without the aerosol cooling. The aerosol cooling (together with subsidence) contributes in suppressing convective venting of the PBL [*Stenchikov et al*., 1998].

We also calculated optical properties and the shortwave radiative forcing at the surface for the other aerosol size distribution measurements on July 15, 1995, available from the Greenbelt site. Table 2 shows the time of measurement, solar zenith angle, radiative parameters (optical depth, single scattering albedo, and asymmetry parameter), and change in net downward shortwave fluxes at the surface using both the calculated single scattering albedo of 0.96 and a single scattering albedo of 1.0 for purely scattering aerosols. When $\omega = 1.0$ is assumed, the shortwave forcing due to aerosols is somewhat weaker, reaching ∼−60 W m^{-2} at the surface, because of increased forward scattering. Purely scattering aerosols, however, are more effective in increasing photolysis rates because of increased actinic fluxes.

A similar effect was reported from the results of the Indian Ocean Experiment (INDOEX), where regionally the aerosol forcing reached −70 W m^{-2} [*Ramanathan*, 1999]. Although the INDOEX observations were over the ocean surface, single-column model calculations show that aerosol radiative forcing affects the diurnal cycle of convection and cloudiness [*Kiehl et al*., 1999].

3.2. Case 2: Convective Formation of Upper Troposphere Pollution Plumes in the Central United States

For case 2 we conduct comparisons of the SCCTM with cloud-resolving calculations to test parameterizations and chemical mechanisms. We focus on the convective event that occurred on June 10–11, 1985, in Kansas-Oklahoma observed during the PRE-STORM campaign. A line of convective cells formed ahead of a surface cold front entering the western region of Kansas and was first seen on radar at ∼2100 UT, June 10, near Garden City, Kansas. This squall line quickly developed, intensified, and moved toward the southeast [*Rutledge et al*., 1988]. This system entered Oklahoma reaching its peak intensity around 0300 UT, June 11 [*Johnson and Hamilton*, 1988]. By 0400 UT it reached Oklahoma City and diminished slightly in intensity. Finally, at 0600 UT on June 11 the squall line was into its dissipating stage. This intense convection was conducive for venting large quantities of boundary layer air, leading to the formation of a pollution plume in the upper troposphere.

This episode was described by *Pickering et al*. [1992b], who mainly focused on the effect of convection on redistribution of chemical species using output from the 2-D Goddard Cumulus Ensemble (GCE) model [*Tao and Simpson*, 1993] for off-line calculations of chemistry with an updated version of the 1-D photochemical model of *Thompson and Cicerone* [1986]. Here we use on-line calculations of chemistry with parameterized vertical transport; we also study the ozone radiative forcing on the regional scale due to the redistribution of ozone precursors and enhanced ozone production in the middle and upper troposphere. We compare our SCCTM calculations with the results from *Pickering et al*. [1992b] since no direct postconvective chemical observations are available for this case. The GCE model simulation of the squall line compared well with radar observations.

Using the same meteorological conditions for June 10–11, 1985, from the GEOS DAS, we conducted two SCCTM simulations based on two different chemical compositions of boundary layer air similar to those used by *Pickering et al*. [1992b]. One represents a rural air simulation at which the grid location is 38.5° in latitude and −101° in longitude (in western Kansas), and the other is at 35.4° in latitude and −98.0° in longitude, representing an urban plume (Oklahoma City) simulation. The ozone precursor emissions used for this calculation were derived from the average of 10 days of OTAG emission data in summer 1995 [*SAI*, 1995]. We conducted calculations with and without the effects of NO_x generated by lightning, such that we can compare transport of NO_x with the results of Pickering et al., who did not include these emissions. We used meteorological conditions from the grid cell with maximum cloud mass flux (40.0°N and 101°W, i.e., where GEOS DAS diagnosed the strongest moist convection) to capture the squall line conditions. The GEOS DAS data show the maximum cloud mass flux (the squall line) moving toward the southeast.

For comparison purposes the same cloud mass fluxes are used for the rural and urban cases, as in the work of *Pickering et al*. [1992b], where the same convective event was simulated with the 2-D GCE model. We use for the initial conditions in the present simulations the profiles of observed species from *Pickering et al*. [1992b].

Because we do not know the detailed large-scale distribution of the chemical species, we calculate the effect of horizontal advection in a diffusion approximation assuming that the large-scale background concentrations outside the region of convection remain constant,

$$\frac{\partial q}{\partial t} = K_{\text{hor}} \frac{\partial^2 q}{\partial X^2}, \tag{5}$$

where q is the constituent mixing ratio.

A subgrid-scale horizontal mixing coefficient (K_{hor}) was computed from the velocity deformation [*Smagorinsky*, 1963; *Deardorff*, 1973],

$$K_{\text{hor}} = 2^{-0.5}(0.14X)^2[(\partial v/\partial x + \partial u/\partial y)^2 + (\partial u/\partial x - \partial v/\partial y)^2]^{0.5}, \tag{6}$$

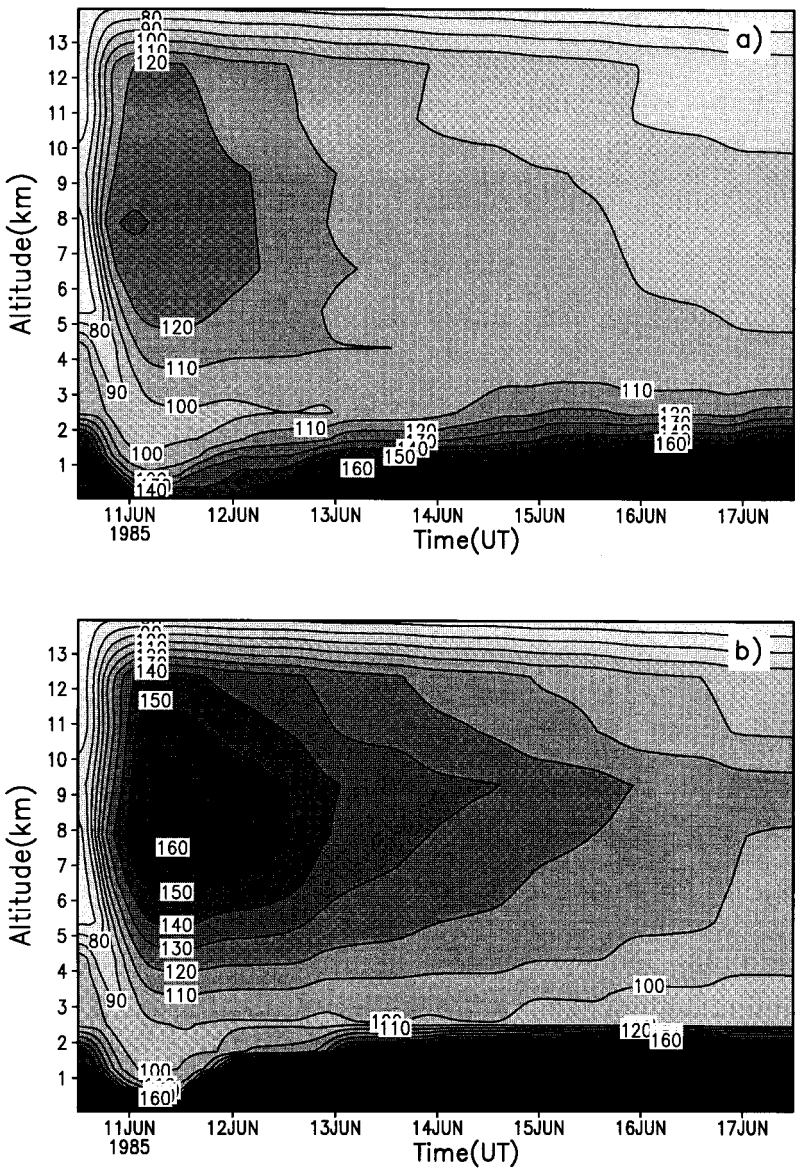

Figure 7. CO tracer analysis simulated with single-column chemical transport model (SCCTM) for (a) rural air and (b) urban plume vertically redistributed in June 10–11, 1985, Kansas/Oklahoma PRESTORM convective event.

where X is the meteorological data grid size and the horizontal winds are defined at the boundary of the grid box. This diffusion approximation of the effect of advection is similar to the nudging term used by *Ghan et al*. [2000] and tends to return the disturbed mixing ratios to the background level. The diffusion coefficient accounts for the horizontal grid spacing and depends on the velocity field.

Clouds as diagnosed by the GEOS-1 DAS are used in both the photolysis rate and radiative forcing calculations. The clouds diagnosed by the assimilation during the July 10–11 convective event are used in the region of convection, whereas average cloud conditions for each 6-hour period over the region downstream of the convection (30–40°N; 70–90°W) are used on the subsequent days. These spatial averages of cloud fraction, when averaged over the 6 days following the convection, were ~0.50–0.55 at altitudes up to ~9 km with values decreasing to ~0.2 at 13 km.

3.2.1. Convective transport of ozone precursors. Figure 7 shows CO mixing ratios simulated with the SCCTM for rural and urban initial conditions. Convective mixing increases CO concentrations in the free troposphere for both cases. The CO mixing ratios reach a peak value at ~8 km for rural conditions (~130 ppbv) and between 7 and 10 km for urban simulations (~160 ppbv) soon after the convection started on June 10–11. Subsequently, the CO mixing ratios decrease with time owing to chemical and advective losses. In the SCCTM simulation we do not calculate any further convective transport after the June 10–11 event such that we can isolate the effect of that event and be compatible with the cloud-resolving calculations conducted by *Pickering et al*. [1992b]. CO mixing ratios in the PBL decrease through convective venting and then following the event increase with time. Our results are in good agreement with those of *Pickering et al*. [1992b] in terms of the maximum CO resulting in the upper troposphere following the convec-

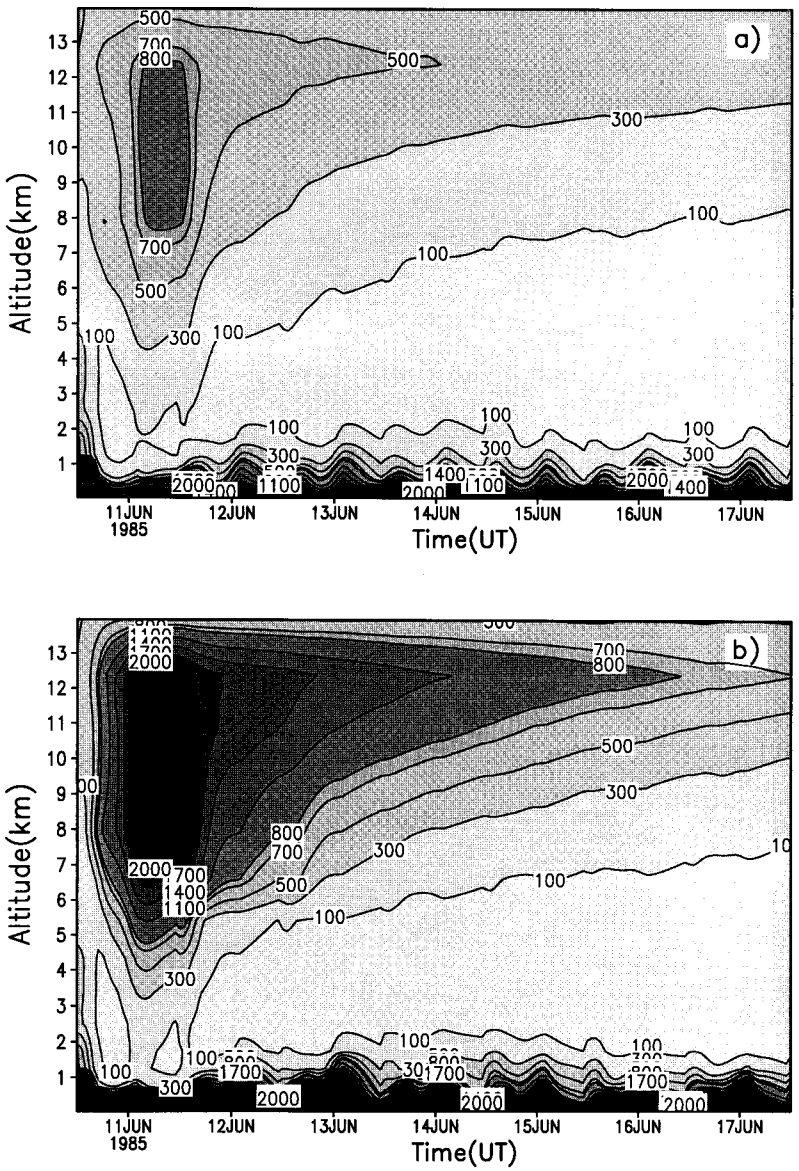

Figure 8. Same as Figure 7 but for NO_x tracer analysis.

tion. However, the peak altitude to which CO from the PBL is transported is lower than that in the work of *Pickering et al*. [1992b]. The 100-ppbv CO mixing ratio for the urban plume in the SCCTM calculations reaches 13 km compared with 15 km in the work of *Pickering et al*. [1992b]. This result suggests that the cloud produced in the GEOS-1 DAS did not penetrate as high as that generated in the cloud-resolving model, also suggested by the profiles of cloud mass flux presented by *Pickering et al*. [1995] for this event from the GEOS-1 DAS and the cloud-resolving model.

Figure 8 shows NO_x calculated for urban and rural initial conditions. In the rural case, NO_x mixing ratios of ~0.8 ppbv result from convective transport in the 8- to 12-km layer, where the typical mixing ratio was initially less than 0.2 ppbv prior to the squall line. In the urban plume simulation the peak NO_x mixing ratio (over 2.0 ppbv) is shown to be between 7 and 12 km after the convection. A mixing ratio of 1 ppbv extends up to ~13 km, which is 2 km lower than that in the cloud-resolving calculations of *Pickering et al*. [1992b]. The maximum NO_x mixing ratios in the upper troposphere calculated by *Pickering et al*. [1992b] (over 1.9 and ~0.7 ppbv for the urban and rural cases, respectively) and in our SCCTM simulations (over 2.0 and 0.8 ppbv for the urban and rural cases, respectively) are in good agreement. In summary, the parameterized convective transport appears to compare quite favorably with that computed with a cloud-resolving model. Slightly less NO_x (<0.1 ppbv) was computed when the wet scavenging algorithm was turned off. This resulted from there being more HO_x available in the no-scavenging run to oxidize NO and NO_2.

3.2.2. Photochemical ozone production in the convective plume. Figure 9 shows the difference in O_3 mixing ratios calculated with and without convection for rural and urban conditions, respectively. Rapid transport of polluted air from the PBL enhances O_3 chemical production between 2 and 10 km immediately after the convection on June 10–11. Transport of lower values of O_3 from the PBL into upper troposphere initially decreases O_3 mixing ratio above 10 km. However, O_3 production soon occurs as convectively transported ozone pre-

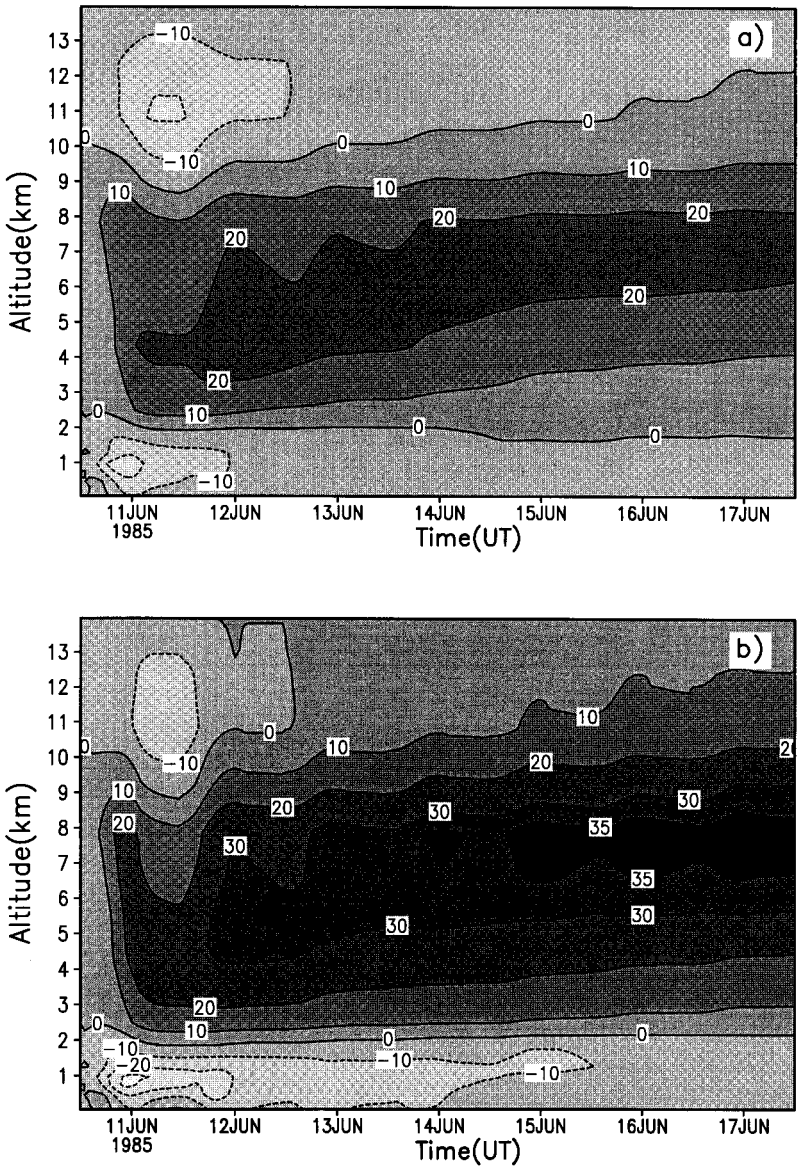

Figure 9. Differences in ozone mixing ratios calculated for (a) rural air and (b) urban plume with convection versus with no convection for June 10–11 PRESTORM convective event.

cursors are chemically processed, and O_3 mixing ratios subsequently increase with time. After 4 days the effect of the June 10–11 convection is to increase O_3 mixing ratio over 35 and 20 ppbv in the middle troposphere for urban and rural conditions, respectively.

The change of O_3 mixing ratio in Figure 9 is relatively uniform in altitude. It is primarily caused by convective mixing of ozone and its precursors. The parameterization of *Chang et al.* [1987] for in-cloud photolysis rates underestimates the decrease of photolysis rates at the bottom of optically thick clouds in comparison with that of *Madronich* [1987]. However, when we modified the parameterization of *Chang et al.* [1987] to approximate the *Madronich* [1987] estimate for optically thick clouds, the change of O_3 mixing ratio appears to be very close to that shown in Figure 9.

In Figure 10 we show that the calculated values of O_3 change as a result of convection for the first 24 hours immediately after the June 10–11 event, as a function of altitude for the urban and rural initial conditions. In the rural simulation, convection increased the rate of ozone production by 5–9 ppbv d^{-1} between 3 and 12 km. A recent cloud model study [*DeCaria et al.*, 2000] shows a similar increase of 7 ppbv d^{-1} in upper tropospheric ozone primarily due to lightning NO_x in an individual thunderstorm. In urban plume conditions, convection results in an increase in the rate of ozone production of 10–18 ppbv O_3 d^{-1}. In our calculations the effect of convection on photochemical ozone production is largest at ~9 km, but *Pickering et al.* [1992b] found that the ozone production rate for the first 24 hours decreased with altitude. This difference may be attributed to the profile of cloud detrainment from the GEOS-1 DAS, which was different from that of the cloud-resolving model. Detrainment in the parameterized convection appeared in all upper layers above 6 km and reaches maximum at 8–9 km. The cloud model shows more detrainment at lower levels. *Pickering et al.* [1992b] conducted calculations for a particular column in the 2-D model field, while in the SCCTM

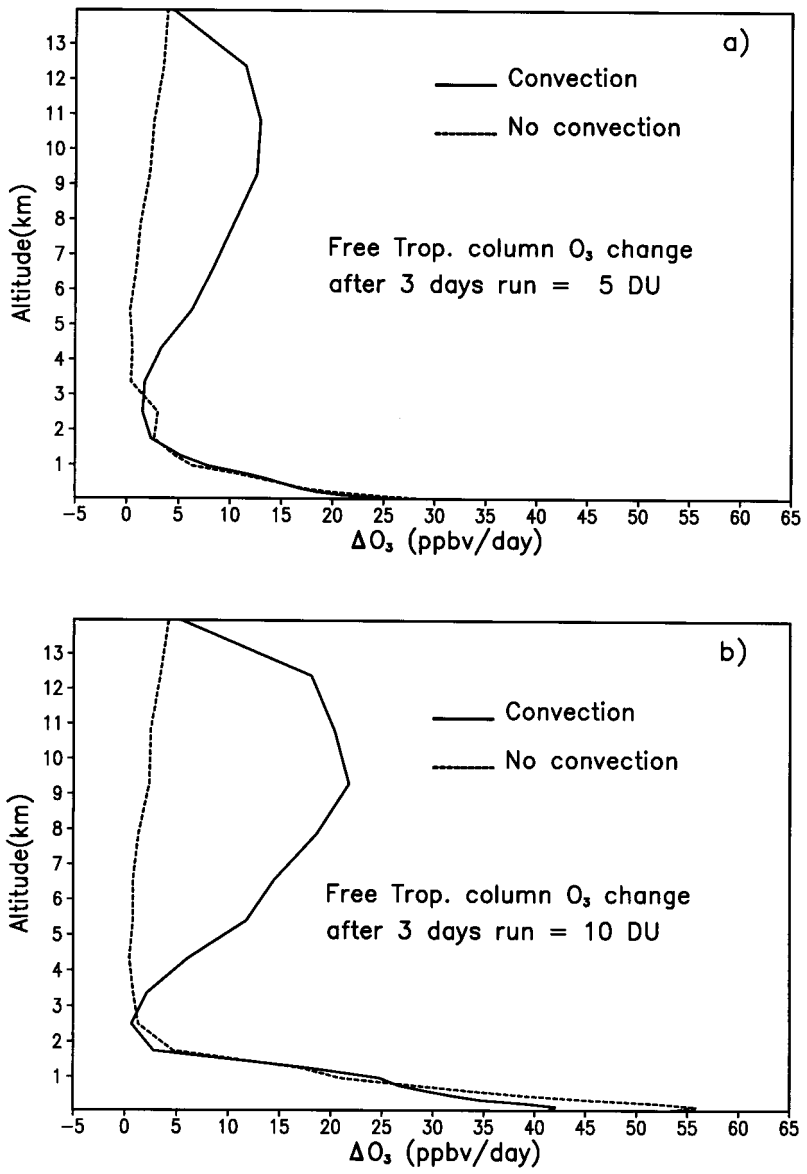

Figure 10. Change in ozone (ppbv d^{-1}) computed from the SCCTM simulations with convection and with no convection for the first 24-hour period following the June 10–11, 1985, Kansas/Oklahoma PRESTORM event for (a) rural air and (b) urban plume conditions.

calculations we use area average convective mass flux from GEOS DAS. The accumulated increases in total column O_3 caused by convection are 5 and 10 DU for the rural and urban cases, respectively, for the 3 days after the June 10–11 convection.

Vertical mixing of pollutants also results in a very significant increase of production of peroxyacetylnitrate (PAN) in the middle and upper troposphere. The results show a quick conversion of NO_x into PAN during the transport to the free troposphere. The peak PAN concentrations (not shown) are 500 and 250–300 pptv for the urban and for the rural condition in the free troposphere, while the typical mixing ratio was 100 pptv prior to the convection. This PAN reservoir for NO_x in the convective plume may contribute significantly to the production of O_3 as it moves further downstream, particularly if adiabatic or radiative warming of the plume occurs.

3.2.3. Effect of lightning NO_x on photochemical ozone production in the convective plume. NO_x mixing ratios in the convective plume were likely larger than what we computed in section 3.2.1 owing to production of NO_x by lightning. Therefore we conducted the case 2 simulations again including lightning NO_x production. For this calculation we used the profile of lightning NO_x calculated by *Pickering et al.* [1998] in the GCE model for the June 10–11 convective event. Total lightning NO_x mixing ratios are gradually added in the SCCTM over the period of convection.

When lightning is included, the peak NO_x mixing ratio becomes 1.7 ppbv (rural) and 3.0 ppbv (urban) in the upper troposphere (not shown). The increment due to lightning is ~1.0 ppbv in both cases. Lightning NO_x further increases O_3 mixing ratios in the free troposphere in the rural simulation. The maximum O_3 increase over the results with no lightning

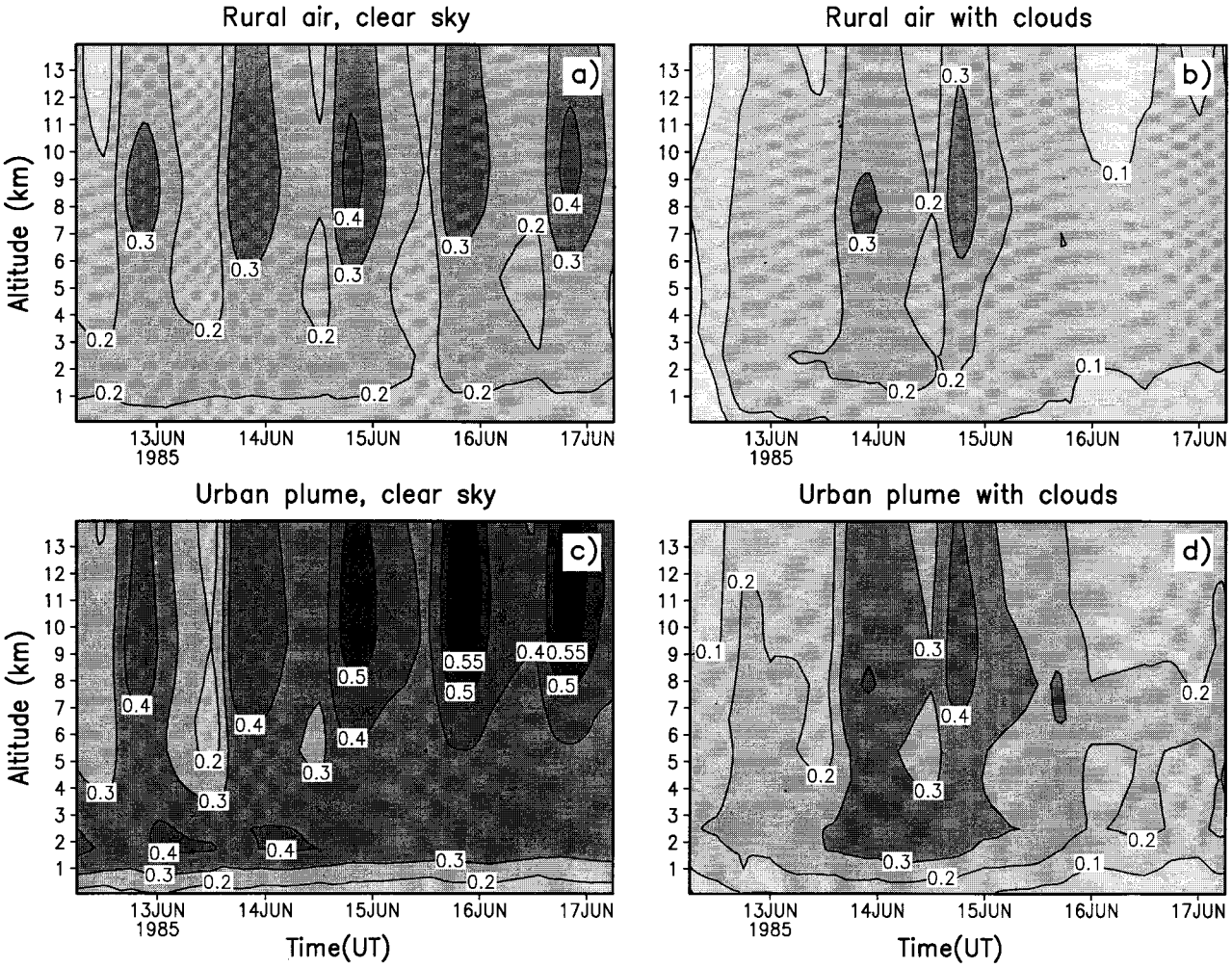

Figure 11. Longwave radiative forcing due to the increases in ozone mixing ratios resulting from the June 10–11, 1985, Kansas/Oklahoma PRESTORM deep convection for (a) rural air clear sky, (b) rural air with clouds, (c) urban plume clear sky, and (d) urban plume with clouds.

NO_x is ~4 ppbv between 5 and 7 km after 5 days. In the urban plume simulation, O_3 production appears to be less efficient (O_3 increment of only 2.5 ppbv) in the middle troposphere. The additional NO_x from lightning caused the O_3 mixing ratio to decrease (peak decrease of −2.0 ppbv around 12 km) in the upper troposphere above 10 km where the largest mixing ratios of lightning NO_x are injected. Inclusion of lightning NO_x in our simulations has variable effects on the ozone production depending on altitude and chemical environment. Under the relatively clean rural conditions, it enhances O_3 production in the free troposphere. Ozone in the urban plume (enriched NO_x because of upward transport from the polluted PBL), however, decreases because of titration by freshly emitted NO in the upper troposphere.

3.2.4. Effect of the convective plume on radiative forcing. We have computed the radiative forcing of the additional ozone produced as a result of the convective transport of polluted air and lightning NO_x for the June 10–11 convective event. The calculations were conducted both for clear-sky conditions and for the average cloud fraction diagnosed by the GEOS-1 DAS on each of the 6 days following the convection over the region downstream at each model level.

Figure 11 shows the instantaneous LW forcing (change in net LW flux, positive direction is downward) due to the changes in O_3 in the free troposphere. The peak increase in net downward LW radiation appears slightly above the peak of O_3. In the rural case the increase of 20 ppbv in upper tropospheric O_3 results in increase of downward LW flux by ~0.4 W m^{-2} in the upper troposphere under the clear-sky assumption and 0.3 W m^{-2} under the average cloudiness assumption. In the urban simulation the radiative forcing reaches a maximum of 0.55 W m^{-2} above 8 km on June 15–16 with clear skies and a maximum of 0.4 W m^{-2} under the average cloud conditions.

Figure 12 shows the instantaneous SW radiative forcing (change in net SW radiative flux, positive direction is downward) for the same case. Increases in net shortwave fluxes are clearly shown above 6 km up to ~14 km (covering the tropopause region) after the June 10–11 convection. This effect is caused by absorption by ozone of reflected and backward scattered solar ultraviolet radiation. The peak increases for rural air exceed 0.15–0.20 W m^{-2} for both clear-sky and average cloud conditions. The peak increases for urban plume exceed 0.25 W m^{-2} for both clear-sky and average cloud conditions. With average cloud conditions the forcing exceeds 0.15 and 0.25 W m^{-2} for the rural and urban simulations. The clear-sky SW forcing is about the same as the cloudy-sky SW forcing

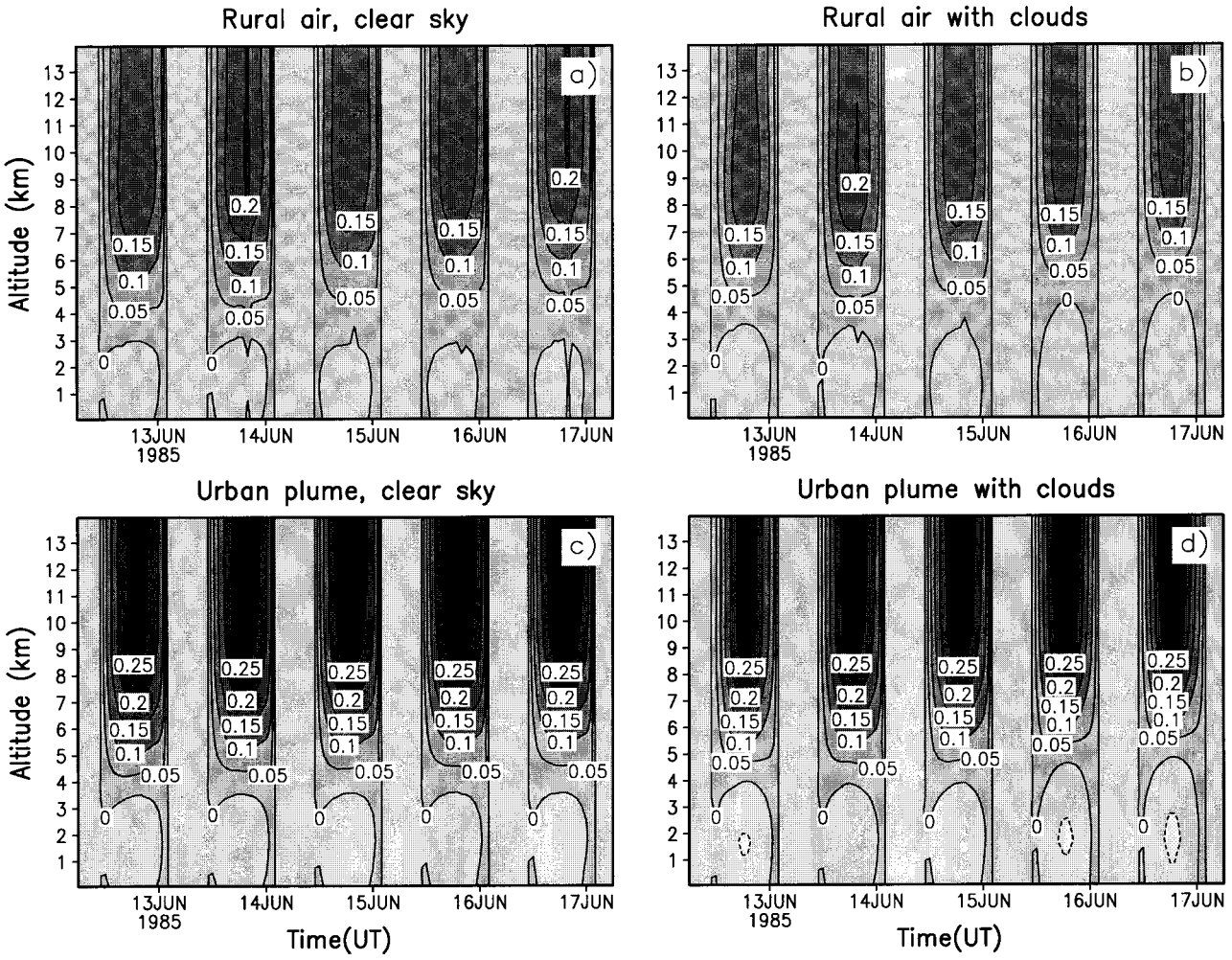

Figure 12. (a–d) Same as Figure 11 but for shortwave radiative forcing.

because although clouds attenuate solar radiation, the increase in photon optical path in the scattering cloudy atmosphere favors ozone absorption.

Both the clear and average cloud calculations show positive total radiative forcing (longwave + shortwave) in the free troposphere and at the tropopause after the June 10–11 convection and also show a strong correlation between the changes in O_3 mixing ratios and radiative forcing in upper troposphere in agreement with *Lacis et al*. [1990] and *Wang et al*. [1993]. Using a general circulation model, *Roelofs* [1999] showed that the effect of clouds is to attenuate the longwave forcing at the tropopause (-0.08 W m^{-2} with instantaneous cloud; -0.06 W m^{-2} with monthly averaged cloud) but slightly increase shortwave forcing at the tropopause (0.04 W m^{-2} with instantaneous cloud; 0.06 W m^{-2} with monthly averaged cloud).

A recent estimate of the global annual average radiative forcing due to changes in greenhouse gases (CO_2, CH_4, N_2O, and the halocarbons) since preindustrial times is 2.45 W m^{-2} [*Houghton et al*., 1996]. Numerous model studies [e.g., *Brasseur et al*., 1998; *Stevenson et al*., 1998; *Haywood et al*., 1998; *Mickley et al*., 1999] have calculated the impact of changes in tropospheric ozone on radiative forcing since preindustrial times. Such estimates range from 0.29 to 0.42 W m^{-2} averaged globally and annually. Furthermore, *Brasseur et al*. [1998] showed radiative forcing of 0.62 W m^{-2} in the Northern Hemisphere during summer. The maximum annual mean clear-sky instantaneous radiative forcing exceeds 0.9 W m^{-2} from the results of *Haywood et al*. [1998]. Our results show that the maximum regional contribution to total (longwave + shortwave) ozone radiative forcing exceeds 0.75 W m^{-2} owing to the increase in upper tropospheric ozone resulting from the urban plume redistribution by the June 10–11 Oklahoma convection (Figures 11 and 12). However, this value is valid only for a region and for a short duration and cannot be directly compared with the literature values cited above. However, it is a nonnegligible amount of radiative forcing, compared with the total ozone effect. Although this result should be considered as an upper limit, it implies a significant role for deep convective mixing in regional- and global-scale chemical budgets and radiative forcing. This result demonstrates that accuracy of deep convective parameterizations is essential in global analyses of radiative forcing and climate response.

To build a bridge from regional to continental and global scales, we have attempted to estimate a regional radiative forcing of the increase in O_3 due to deep convection for the central United States (32.5°–50°N, 90°–105°W) as defined by *Thompson et al*. [1994] for the month of June. Based on the International Satellite Cloud Climatology Project (ISCCP) [*Rossow and Schiffer*, 1991], average deep convective cloud coverage for this region was estimated for the Junes of 1984

through 1990. Our clear-sky estimate of total (longwave + shortwave) free tropospheric radiative forcing of O_3 24 hours after the June 10–11 convective event is 0.375 W m^{-2}, averaged over the rural and urban cases. We extrapolate this increase in energy to the central United States by multiplying this radiative forcing by the average fraction of area covered with convective plumes. From ISCCP we know that the average deep convective cloud cover is 7.9%. We assume that cloud outflow plumes extend over an area 3–5 times as large as the convective regions themselves at the end of 24 hours of transport [*Thompson et al*., 1994]. If these factors are applied, the regional radiative forcing averaged over the month is calculated to be between 0.09 and 0.15 W m^{-2}. We consider these estimates as minimum values because of the probable underestimate of deep convective cloud cover by ISCCP [*Klein and Hartmann*, 1993] and, moreover, because the convective plumes over the central United States persist for longer than 24 hours.

4. Conclusions

Using the SCCTM we have conducted two case study calculations and tested the employed parameterizations and physical schemes. In each case we performed analyses of the effects of various atmospheric processes and investigated the sensitivity of the model results to model input parameters, particularly focusing on convection and aerosols. In agreement with the previous investigations, we found that typically observed east coast U.S. aerosols (case 1) tend to increase the photochemical ozone production in the PBL owing to increased photolysis rates and the possible suppression of convection. The effect on O_3 production of heterogeneous loss of N_2O_5 on aerosol is comparable in magnitude and opposite in sign with the radiative effect of aerosols on photolysis rates. In the central United States (case 2), ozone production in the upper and middle troposphere was enhanced following deep convective transport of pollution and lightning NO_x. Radiative forcing of observed aerosols (case 1) and chemically produced ozone (case 2) appears to be significant at least on a regional scale. Specific findings are as follows.

1. In the East Coast urban simulation (case 1) the calculated O_3 mixing ratios are in reasonable agreement with the ozone measurements at the Greenbelt, Maryland, site. The results show strong sensitivity of calculated surface O_3 to aerosol optical depth and aerosol vertical distribution (depth of the aerosol layer).

2. Interactive calculations with a diurnally varying vertical distribution of aerosols showed that this effect causes significant time variation of the vertical profiles of the photolysis rates and, in combination with the vertical distribution of ozone precursors and the diurnal cycle of solar radiation, could significantly affect ozone production. Ozone production at the surface can be either increased or decreased, depending on the depth of the aerosol layer. However, vertically averaged ozone mixing ratios in the PBL were larger on all days in the simulation with aerosols than in the simulation without aerosols.

3. In the central U.S. convection simulation (case 2) we showed that convective mixing and lightning NO_x production result in major changes in the profiles of ozone precursors and hence increase free tropospheric O_3 by up to 35 ppbv and PAN by up to 400 pptv for urban plume conditions.

4. The results of convective mixing calculations using the SCCTM parameterizations are in good agreement with cloud-resolving calculations of *Pickering et al*. [1992b]. The top of the cloud in the GEOS-1 DAS (and hence in the SCCTM), however, is lower than that obtained with the cloud-resolving model, which compared favorably with observations. The SCCTM cloud detrained more ozone precursors at higher altitude than in the cloud-resolving model, which affects the vertical profile of resulting ozone production rates.

5. Use of retrieved aerosol optical properties in our SCCTM radiative transfer calculations for the East Coast urban case showed that net downward shortwave flux decreases up to 100 W m^{-2} near the surface, and the peak increase in net longwave flux reaches 4.5 W m^{-2} in the PBL. In spite of reduced radiation reaching the surface, the actinic flux increases in the upper part of the PBL, resulting in the increases in O_3 production in that region.

6. We showed that deep convection on June 10–11, 1985, in the central United States (case 2) not only causes changes in the chemical budget in the troposphere but also produces a significant total radiative forcing (maximum 0.75 W m^{-2}), which may have impacts on regional atmospheric dynamics.

Our results have demonstrated that estimation of boundary layer ozone production over polluted areas in photochemical models is very sensitive to inclusion of aerosol and that it is critical that the model accurately represent the boundary layer depth. We also found that accurate representation of parameterized convective transport is essential in model analyses of radiative forcing by tropospheric ozone. The results of our two dissimilar case studies have demonstrated that the parameterizations and chemical mechanism in the SCCTM perform reasonably well in comparison with observations and cloud-resolving model calculations. However, more observations are needed to conduct further detailed testing of chemical mechanisms. We will use the algorithms developed for the SCCTM in 3-D transport and coupled GCM simulations.

Acknowledgments. We thank Brent Holben for providing aerosol data and Anne Thompson for valuable discussions. This work was supported through a NASA EOS Interdisciplinary Science Investigation under NASA grant NAG5-3678. Measurements in the Baltimore-Washington area were supported by the Maryland Dept. of the Environment and the Maryland Dept. of Natural Resources.

References

Allen, D. J., P. Kasibhatla, A. M. Thompson, R. B. Rood, B. G. Doddridge, K. E. Pickering, R. D. Hudson, and S.-J. Lin, Transport-induced interannual variability of carbon monoxide determined using a chemistry and transport model, *J. Geophys. Res*., *101*, 28,655–28,669, 1996.

Allen, D., K. Pickering, G. Stenchikov, A. Thompson, and Y. Kondo, A three-dimensional total odd nitrogen (NO_y) simulation during SONEX using a stretched-grid chemical transport model, *J. Geophys. Res*., *105*, 3851–3876, 2000.

Arakawa, A., and W. H. Schubert, Interaction of a cumulus cloud ensemble with the large-scale environment, part I, *J. Atmos. Sci*., *31*, 674–701, 1974.

Atkinson, R., D. L. Baulch, R. A. Cox, R. F. Hampson Jr., J. A. Kerr, M. J. Rossi, and J. Troe, Evaluated kinetic photochemical and heterogeneous data for atmospheric chemistry: Supplement V, *J. Phys. Chem. Ref. Data*, *26*, 521 pp., 1997.

Brasseur, G. P., J. Kiehl, J. F. Muller, T. Schneider, C. Cranier, X. Tie, and D. Hauglustaine, Past and future changes in global tropospheric ozone: Impact on radiative forcing, *Geophys. Res. Lett*., *25*, 3807–3810, 1998.

Chang, J. S., R. A. Brost, I. S. A. Isaksen, S. Madronich, P. Middleton, W. R. Stockwell, and C. J. Walcek, A three-dimensional Eulerian acid deposition model: Physical concepts and formulation, *J. Geophys. Res*., *92*, 14,681–14,700, 1987.

Charlson, R. J., S. E. Schwartz, J. M. Hales, R. D. Cess, J. A. Coakley Jr., J. E. Hansen, and D. J. Hofmann, Climate forcing by anthropogenic aerosols, *Science*, *255*, 423–429, 1992.

Chatfield, R. B., and A. C. Delany, Convection links biomass burning to increased tropical ozone: However, models will tend to overpredict O_3, *J. Geophys. Res*., *95*, 18,473–18,488, 1990.

Chou, M.-D., A solar radiation model for use in climate studies, *J. Atmos. Sci*., *49*, 762–772, 1992.

Chou, M.-D., and M. Suarez, An efficient thermal infrared radiation parameterization for use in general circulation models, *NASA Tech. Memo*., *104606*, Vol. 3, 85 pp., 1994.

Chou, M.-D., W. L. Ridgway, and M. M.-H. Yan, Parameterization for water vapor IR radiative transfer in both the middle and lower atmosphere, *J. Atmos. Sci*., *52*, 1159–1167, 1995.

Coulson, K. L., and D. W. Reynolds, The spectral reflectance of natural surfaces, *J. Appl. Meteorol*., *10*, 1285–1295, 1971.

Deardorff, J. W., Three-dimensional numerical modeling of the planetary boundary layer, in *Workshop on Meteorology*, edited by D. A. Haugen, pp. 271–311, Am. Meteorol. Soc., Boston, Mass., 1973.

DeCaria, A. J., K. E. Pickering, G. L. Stenchikov, J. R. Scala, J. L. Stith, J. E. Dye, B. A. Ridley, and P. Laroche, A cloud-scale model study of lightning-generated NO_x in an individual thunderstorm during STERAO-A, *J. Geophys. Res*., *105*, 11,601–11,616, 2000.

DeMore, W. B., S. P. Sander, D. M. Golden, M. J. Molina, R. F. Hampson, M. J. Kurylo, C. J. Howard, and A. R. Ravishankara, Chemical kinetics and photochemical data for use in stratospheric modeling, *JPL Publ*., *97-4*, 1997.

Dickerson, R. R., D. H. Stedman, and A. C. Delany, Direct measurements of ozone and nitrogen dioxide photolysis rates in the troposphere, *J. Geophys. Res*., *87*, 4933–4946, 1982.

Dickerson, R. R., S. Kondragunta, G. Stenchikov, K. L. Civerolo, B. G. Doddridge, and B. N. Holbel, The impact of aerosols on solar ultraviolet radiation and photochemical smog, *Science*, *278*, 827–830, 1997.

Fox-Rabinovitz, M. S., G. L. Stenchikov, M. J. Suarez, and L. L. Takacs, A finite-difference GCM dynamical core with a variable resolution stretched grid, *Mon. Weather Rev*., *125*, 2943–2968, 1997.

Fox-Rabinovitz, M. S., L. L. Takacs, and M. J. Suarez, A variable resolution stretched grid GCM: Regional climate simulation, *Mon. Weather Rev*., in press, 2001.

Gamazaychikov, M., G. Stenchikov, M. Fox-Rabinovitz, R. Dickerson, and K. Pickering, Aerosol radiative effects on dynamical mixing and chemical processes in the planetary boundary layer, *Eos Trans. AGU*, *79*(17), Spring Meet. Suppl., S34, 1998.

Gery, M. W., G. Z. Whitten, J. P. Killus, and M. C. Dodge, A photochemical kinetics mechanism for urban and regional scale computer modeling, *J. Geophys. Res*., *94*, 12,925–12,956, 1989.

Ghan, S., et al., A comparison of single column model simulations of summertime midlatitude continental convection, *J. Geophys. Res*., *105*, 2091–2124, 2000.

Haigh, J. D., The impact of solar variability on climate, *Science*, *272*, 981–984, 1996.

Haywood, J. M., M. D. Schwarzkopf, and V. Ramaswamy, Estimates of radiative forcing due to modeled increases in tropospheric ozone, *J. Geophys. Res*., *103*, 16,999–17,007, 1998.

Hegg, D. A., J. Livingston, P. V. Hobbs, T. Novakov, and P. Russell, Chemical apportionment of aerosol column optical depth off the mid-Atlantic coast of the United States, *J. Geophys. Res*., *102*, 25,293–25,303, 1997.

Helfand, H. M., M. Fox-Rabinovitz, L. Takacs, and A. Molod, Simulation of the planetary boundary layer and turbulence in the GLA GCM, paper presented at Ninth Conference on Numerical Weather Prediction, Am. Meteorol. Soc., Denver, Colo., 1991.

Holben, B. N., et al., AERONET: A federated instrument network and data archive for aerosol characterization, *Remote Sens. Environ*., *66*, 1–16, 1998.

Houghton, J. T., L. G. Meira Filho, B. A. Callander, N. Harris, A. Kattenberg, and K. Maskell, *Climate Change 1995: The Science of Climate Change*, Cambridge Univ. Press, New York, 1996.

Jacob, D. J., Heterogeneous chemistry and tropospheric ozone, *Atmos. Environ*., *34*, 2131–2159, 2000.

Jacobson, M. Z., Developing, coupling, and applying a gas, aerosol, transport, and radiation model to study urban and regional air pollution, Ph.D. thesis, Univ. of Calif., Los Angeles, 1994.

Jacobson, M. Z., Computation of global photochemistry with SMVGEAR II, *Atmos. Environ*., *29*, 2541–2546, 1995.

Jacobson, M. Z., Development and application of a new air pollution modeling system, part III, Aerosol phase simulations, *Atmos. Environ*., *31*, 587–608, 1997.

Jacobson, M. Z., Studying the effects of aerosols on vertical photolysis rate coefficient and temperature profiles over an urban airshed, *J. Geophys. Res*., *103*, 10,593–10,604, 1998.

Johnson, R. H., and P. J. Hamilton, The relationship of surface pressure features to the precipitation and airflow structure of an intense midlatitude squall line, *Mon. Weather Rev*., *116*, 1444–1472, 1988.

Kelley, P., R. R. Dickerson, W. T. Luke, and G. L. Kok, Rate of NO_2 photolysis from the surface to 7.6 km altitude in clear-sky and clouds, *Geophys. Res. Lett*., *22*, 2621–2624, 1995.

Kiehl, J. T., and B. P. Briegleb, The relative role of sulfate aerosols and greenhouse gases in climate forcing, *Science*, *260*, 311–314, 1993.

Kiehl, J. T., V. Ramanathan, J. J. Hack, A. Huffman, and K. Swett, The role of aerosol absorption in determining the atmospheric thermodynamic state during INDOEX, *Eos Trans. AGU*, *80*(46), Fall Meet. Suppl., F183, 1999.

Klein, S. A., and D. L. Hartmann, Spurious changes in the ISCCP dataset, *Geophys. Res. Lett*., *20*, 455–458, 1993.

Kondragunta, S., The impact of aerosols on urban photochemical ozone production, Ph.D. dissertation, Dept. of Chem., Univ. of Md., 230 pp., 1997.

Kurucz, R. L., I. Furenlid, J. Brault, and L. Testerman, Solar flux atlas from 296 to 1300 nm, *Atlas 1*, Natl. Sol. Obs., Sunspot, N. M., 1984.

Lacis, A. A., D. J. Wuebbles, and J. A. Logan, Radiative forcing of climate by changes in the vertical distribution of ozone, *J. Geophys. Res*., *95*, 9971–9981, 1990.

Lelieveld, J., and P. J. Crutzen, Role of deep cloud convection in the ozone budget of the troposphere, *Science*, *264*, 1759–1761, 1994.

Liao, H., Y. L. Yung, and J. H. Seinfeld, Effects of aerosols on tropospheric photolysis rates in clear and cloudy atmospheres, *J. Geophys. Res*., *104*, 23,697–23,707, 1999.

Lin, S.-J., and R. B. Rood, Multidimensional flux-form semi-Lagrangian transport schemes, *Mon. Weather Rev*., *124*, 2046–2070, 1996.

Liou, K. N., *Radiation and Cloud Processes in the Atmosphere*, 166 pp., Oxford Univ. Press, New York, 1992.

Liu, S. C., M. Trainer, F. C. Fehsenfeld, D. D. Parrish, E. J. Williams, D. W. Fahey, G. Hubler, and P. C. Murphy, Ozone production in the rural troposphere and the implications for regional and global ozone distributions, *J. Geophys. Res*., *92*, 4191–4207, 1987.

Madronich, S., Photodissociation in the atmosphere, 1, Actinic flux and the effects of ground reflections and cloud, *J. Geophys. Res*., *92*, 9740–9752, 1987.

Manabe, S., and R. T. Wetherald, Thermal equilibrium of the atmosphere with a given distribution of relative humidity, *J. Atmos. Sci*., *24*, 241–259, 1967.

Mickley, L. J., P. P. Murti, D. J. Jacob, J. A. Logan, D. M. Koch, and D. Rind, Radiative forcing from tropospheric ozone calculated with a unified chemistry-climate model, *J. Geophys. Res*., *104*, 30,153–30,172, 1999.

Molina, L. T., and M. J. Molina, Absolute absorption cross section of ozone in the 185- to 350-nm wavelength range, *J. Geophys. Res*., *91*, 14,501–14,508, 1986.

Moorthi, S., and M. J. Suarez, Relaxed Arakawa-Schubert: A parameterization of moist convection for general circulation models, *Mon. Weather Rev*., *120*, 978–1002, 1992.

Penner, J. E., C. C. Chuang, and K. Grant, Climate forcing by carbonaceous and sulfate aerosols, *Clim. Dyn*., *14*, 839–851, 1998.

Pickering, K. E., A. M. Thompson, R. R. Dickerson, W. T. Luke, D. P. McNamara, J. P. Greenberg, and P. R. Zimmerman, Model calculations of tropospheric ozone production potential following observed convective events, *J. Geophys. Res*., *95*, 14,049–14,062, 1990.

Pickering, K. E., J. R. Scala, A. M. Thompson, W.-K. Tao, and J. Simpson, A regional estimate of convective transport of CO from biomass burning, *Geophys. Res. Lett*., *19*, 289–292, 1992a.

Pickering, K. E., A. M. Thompson, J. R. Scala, W.-K. Tao, R. R. Dickerson, and J. Simpson, Free tropospheric ozone production following entrainment of urban plumes into deep convection, *J. Geophys. Res*., *97*, 17,985–18,000, 1992b.

Pickering, K. E., A. M. Thompson, W.-K. Tao, R. B. Rood, D. P. McNamara, and A. M. Molod, Vertical transport by convective clouds: Comparisons of three modeling approaches, *J. Geophys. Res*., *22*, 1089–1092, 1995.

Pickering, K. E., Y. Wang, W.-K. Tao, C. Price, and J.-F. Muller,

Vertical distributions of lightning NO_x for use in regional and global chemical transport models, *J. Geophys. Res*., *103*, 31,203–31,216, 1998.

Ramanathan, V., The role of the ocean-atmosphere interaction in the CO_2 climate problem, *J. Atmos. Sci*., *38*, 918–930, 1981.

Ramanathan, V., The Indian Ocean Experiment: An overview of the aerosol climate forcing with implications to climate change, *Eos Trans. AGU*, *80*(46), Fall Meet. Suppl., F160, 1999.

Randall, D. A., K.-M. Xu, R. J. C. Sommerville, and S. Iacobellis, Single-column models and cloud ensemble models as links between observations and climate models, *J. Clim*., *9*, 1683–1697, 1996.

Roelofs, G.-J., Radiative forcing by tropospheric ozone: Impact of cloud representation, *Geophys. Res. Lett*., *26*, 467–470, 1999.

Rossow, W. B., and R. A. Schiffer, International Satellite Cloud Climatology Project (ISCCP) cloud data products, *Bull. Am. Meteorol. Soc*., *72*, 2–20, 1991.

Rutledge, S. A., R. A. Houze Jr., M. I. Biggerstaff, and T. Matejka, The Oklahoma-Kansas mesoscale convective system of 10–11 June 1985: Precipitation structure and single-Doppler radar analysis, *Mon. Weather Rev*., *116*, 1409–1430, 1988.

Ryan, W. F., B. G. Doddridge, R. R. Dickerson, R. M. Morales, K. A. Hallock, P. T. Roberts, D. L. Blumenthal, J. A. Anderson, and K. L. Civerolo, Pollutant transport during a regional O_3 episode in the mid-Atlantic states, *J. Air Waste Manage. Assoc*., *48*, 786–797, 1998.

SAI, User's guide to the variable-grid urban airshed model (UAM-V), *Tech. Rep. SYSAPP-95/027*, Syst. Appl. Int., San Rafael, Calif., 1995.

Sander, R., and P. J. Crutzen, Model study indicating halogen activation and ozone destruction in polluted air masses transported to the sea, *J. Geophys. Res*., *101*, 9121–9138, 1996.

Schubert, S., J. Pfaendtner, and R. Rood, An assimilated data set for earth science applications, *Bull. Am. Meteorol. Soc*., *74*, 2331–2342, 1993.

Smagorinsky, J., General circulation experiments with the primitive equations, 1, The basic experiment, *Mon. Weather Rev*., *91*, 99–164, 1963.

Stamnes, K., S.-C. Tsay, W. Wiscombe, and K. Jayaweera, Numerically stable algorithm for discrete-ordinate method radiative transfer in multiple scattering and emitting layered media, *Appl. Opt*., *27*, 2502–2509, 1988.

Stenchikov, G. L., and A. Robock, Diurnal asymmetry of climatic response to increased CO_2 and aerosols: Forcings and feedbacks, *J. Geophys. Res*., *100*, 26,211–26,227, 1995.

Stenchikov, G., S. Gray, M. Gamazaychikov, R. Park, and A. Robock, The study of regional climate and chemical processes with single column model, paper presented at Eighth Atmospheric Radiation Measurement (ARM) Science Team Meeting, Tucson, Ariz., March 23–27, 1998.

Stevenson, D. S., C. E. Johnson, W. J. Collins, R. G. Derwent, and K. P. Shine, Evolution of tropospheric ozone radiative forcing, *Geophys. Res. Lett*., *25*, 3819–3822, 1998.

Takacs, L. L., A. Molod, and T. Wang, Documentation on Goddard Earth Observing System (GEOS) General Circulation Model–Version 1, *NASA Tech. Memo*., *104606*, 97 pp., 1994.

Tao, W.-K., and J. Simpson, Goddard Cumulus Ensemble Model, I, Model description, *Terr. Atmos. Oceanic Sci*., *4*, 35–72, 1993.

Thompson, A. M., and R. J. Cicerone, Possible perturbations to atmospheric CO, CH_4, and OH, *J. Geophys. Res*., *91*, 10,853–10,864, 1986.

Thompson, A. M., K. E. Pickering, R. R. Dickerson, W. G. Ellis Jr., D. J. Jacob, J. R. Scala, W.-K. Tao, D. P. McNamara, and J. Simpson, Convective transport over the central United States and its role in regional CO and ozone budgets, *J. Geophys. Res*., *99*, 18,703–18,711, 1994.

VanHoosier, M. E., J.-D. F. Bartoe, G. E. Brueckner, and D. K. Prinz, Absolute solar spectral irradiance 120–400 μm: Results from the Solar Ultraviolet Spectral Irradiance Monitor–SUSIM–experiment on board Spacelab 2, *Astrophys. Lett.*, *27*, 163–168, 1988.

Wang, W.-C., J. P. Pinto, and Y. L. Yung, Climatic effects due to halogenated compounds in the Earth's atmosphere, *J. Atmos. Sci*., *37*, 333–338, 1980.

Wang, W.-C., Y.-C. Zhuang, and R. D. Bojkov, Climate implications of observed changes in ozone vertical distributions at middle and high latitudes of the northern hemisphere, *Geophys. Res. Lett*., *20*, 1567–1570, 1993.

Wang, Y., S. C. Liu, H. Yu, S. T. Sandholm, T.-Y. Chen, and D. R. Blake, Influence of convection and biomass burning outflow on tropospheric chemistry over the tropical Pacific, *J. Geophys. Res*., *105*, 9321–9334, 2000.

Warneck, P., *Chemistry of the Natural Atmosphere*, Academic, San Diego, Calif., 1988.

Wayne, R. P., et al., The nitrate radical: Physics, chemistry, and the atmosphere, *Atmos. Environ*., *25A*, 1–203, 1991.

Wellemeyer, C. G., S. L. Taylor, C. J. Seftor, R. D. McPeters, and P. K. Bhartia, A correction for total ozone maping spectrometer profile shape errors at high latitude, *J. Geophys. Res*., *102*, 9029–9038, 1997.

Wiscombe, W., Improved Mie scattering algorithms, *Appl. Opt*., *19*, 1505–1509, 1980.

D. J. Allen, R. R. Dickerson, R. J. Park, and K. E. Pickering, Department of Meteorology, University of Maryland, College Park, MD 20742, USA.

S. Kondragunta, Office of Research and Applications, NOAA/NESDIS, 5200 Auth Rd., Camp Springs, MD 20746, USA.

G. L. Stenchikov, Department of Environmental Sciences, Rutgers University, 14 College Farm Road, New Brunswick, NJ 08901-8551, USA. (gera@envsci.rutgers.edu)

(Received August 14, 2000; revised April 3, 2001;
accepted July 18, 2001.)